# Further development of a XUV detector for spectroscopy measurements at the experimental storage ring at GSI

**Christian Egelkamp**

Master thesis

June 30, 2016

Institut für Kernphysik
Mathematisch-Naturwissenschaftliche Fakultät
Westfälische Wilhelms-Universität Münster

Referent: Dr. V. Hannen

Koreferent: Prof. Dr. A. Khoukaz

Hiermit versichere ich, dass die vorliegende Arbeit mit dem Titel **"Further development of a XUV detector for spectroscopy measurements at the experimental storage ring at GSI"** selbstständig verfasst worden ist, dass keine anderen Quellen und Hilfsmittel als die angegebenen benutzt worden sind und dass die Stellen der Arbeit, die anderen Werken - auch elektronischen Medien - dem Wortlaut oder Sinn nach entnommen wurden, auf jeden Fall unter Angabe der Quelle als Entlehnung kenntlich gemacht worden sind.

Ort, Datum | Unterschrift

Ich erkläre mich mit einem Abgleich der Arbeit mit anderen Texten zwecks Auffindung von Übereinstimmungen sowie mit einer zu diesem Zweck vorzunehmenden Speicherung der Arbeit in einer Datenbank einverstanden.

Ort, Datum | Unterschrift

für meinen
Opa

# Contents

# 1 Motivation

## 1.1 Highly charged ions

The interest in the structure and the dynamics of highly charged ions largely grew in the recent years. Not only theorists, but also experimentalists show a great interest in the understanding of highly charged ions as they appear for example in plasma physics or astrophysics [1]. They can be used to determine physical conditions within a plasma or an astrophysical object [2]. In theory these ions are of major interest due to the small amount of electrons in the shell and the significant differences compared to their neutral partners. As the extend of the wave function decreases with higher nuclear charge, the probability for the electrons to be close to the nuclei grows significantly resulting in higher electron densities. The thereby created inner electric fields are higher than those accessible by modern high intensity lasers [3]. Due to the higher fields and tighter bound electrons, relativistic effects become stronger and have to be taken into account by theoretical models [4]. The energy difference between the states grows and thus the spectra of these ions are shifted to the ultraviolet or x-ray region.

Current technology opens the field for a wide study of all ionization states for any natural element up to Uranium [5]. This enables the experimental investigation and thus gives an opportunity to test modern atomic theory [6]. In the framework of highly charged ions, beryllium-like atoms take a unique position. Their level scheme contains a fine structure transition from a metastable $^3P_0$ state to the $^3P_1$ state that is largely unaffected by QED corrections and therefore suitable to study effects of relativity and correlation within the electron shell. The lifetime of the metastable statee may be considered infinite [7] and thus allows precise spectroscopy measurements in storage rings.

## 1.2 Laser spectroscopy experiments

Lasers provide the opportunity for precise measurements of atomic transitions [8]. Due to the narrow bandwidth, transition energies can be measured with high precision. Furthermore, pulsed lasers allow the investigation of lifetimes of these transitions. In combination with particle accelerators these studies can be extended to transitions which are normally not accessible by common laser systems. By exploiting the Lorentz boost through a collinear or anti-collinear arrangement of the laser and the ion beam, the excitation wavelengths can be shifted to the desired region. Various experiments with rare isotopes and highly charged ions were carried out in the past [9].

Long living metastable states provide a good opportunity for the investigation of of transitions that are otherwise difficult to access as they do not decay immediately after their production. Beryllium-like ions in the metastable state have almost infinite lifetimes compared to their storage time in the ring. They can be investigated in an anti-collinear laser spectroscopy experiment at relativistic velocities and thus provides a good basis for testing atomic theory.

This thesis will deal with the optimization of a detector for the measurement of the emitted fluorescence photons from laser-excited beryllium-like krypton ions. Therefore, the work will give an introduction about the experimental setting and the physical processes which are important for the detector setup in chapter 2 and 3. After introducing the already existing setup, the discussion extends to possible optimizations of the detector parts in chapter 4. A simulation program is developed and tested with several measurements performed in the laboratory in Münster, to produce reliable results for improving the detector parts. The simulations and measurements are presented in chapter 5 and 6. The main part of the thesis will be about the optimization processes as well as their results in chapter 7. In conclusion, there will be a short summary with an outlook over the next steps and measurements including a test beam time with carbon ions and the actual experiment with krypton.

# 2 The experiment E104

The purpose of the experiment E104 is to measure the transition wavelength between the $^3P_0$ and the $^3P_1$ state in beryllium-like krypton ($^{84}Kr^{32+}$) at the experimental storage ring at GSI to examine electron-electron correlations and relativistic effects. Krypton is a medium Z element with an effective nuclear charge of $Z = 36$. By removing 32 electrons, the remaining electrons form a highly charged beryllium-like ion in a four electron configuration. This system has a stable $1s^2 2s^2$ ground state and also a metastable $1s^2 2s^1 2p^1$ configuration. The $^3P_0$ level is the metastable state with almost infinite lifetime compared to the ion storage time in the ESR. It is in the order of $1 \times 10^7$ s. The transition energy between the $^3P_0$ and the $^3P_1$ state is calculated by different authors via the Multi-Configuration Dirac-Fock method and is in the order of 10.5 eV [10][7]. Figure 1 shows the level scheme of $^{84}Kr^{32+}$ with the $^3P$ fine structure splitting and indications for the relevant transitions in the experiment.

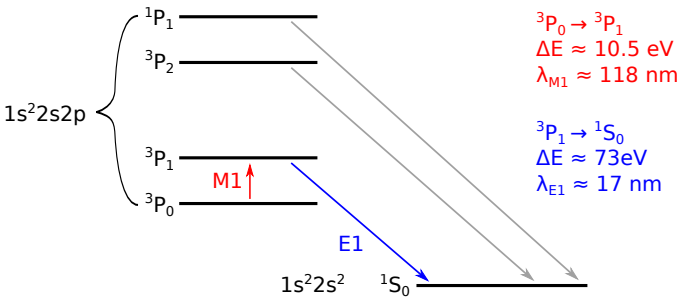


**Figure 1:** Level scheme for beryllium-like Krypton ($^{84}Kr^{32+}$) with the relevant states and transitions according to [11].

The system is investigated via a two photon channel in which the ions are excited from the metastable state via a M1 transition to the $^3P_1$ state. Afterwards the system immediately decays ($\approx 1$ ns) to the $^1S_0$ ground state under the emission of a XUV photon. The photons produced in this E1 decay have a wavelength of 17 nm. Since the excitation wavelength of 118 nm, corresponding to the transition energy of 10.5 eV, cannot be accessed by common laser systems, the ions are accelerated and stored at relativistic velocities of $\beta = 0.69$. By an anti-collinear arrangement between ion beam and a laser, the necessary excitation wavelength can be shifted to approximately 276 nm.

The ESR has a circumference of about 108 m. As shown in figure 2, the ring consists of

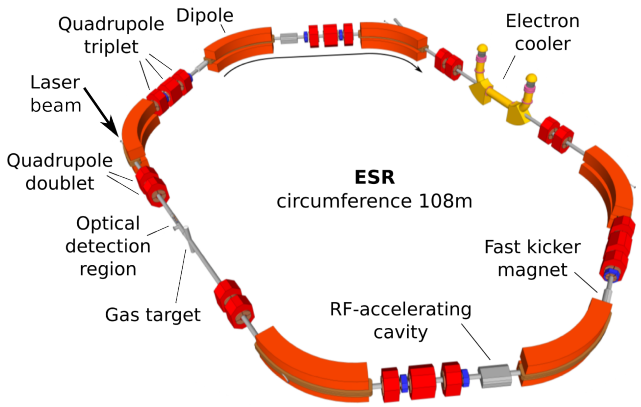


**Figure 2:** Schematic view of the experimental storage ring at GSI with denotations for the main components [12] including the optical detection region where the experiment will be performed.

six dipole magnets which generate magnetic fields up to 1.6 T to bend the ions around the ring curvature with a maximum bending power of 10 T m. In the straight passages between the dipole magnets there are different lens arrangements consisting of quadrupole or sextupole magnets to focus the ion beam. For a sharper energy distribution and thereby better beam quality an electron cooler is installed. Via electrons, which are accelerated to the desired velocity and injected into the beam line, the ions are cooled down to an energy uncertainty smaller than $1 \times 10^{-4}$ [13]. To reduce collisions with residual gas molecules there are ultra high vacuum conditions in the beam pipe in the order of $1 \times 10^{-11}$ mbar. Also, indicated at the left side of the picture is the optical detection region where the detector that is optimized in the course of this work will be mounted for the experiment. The ions are injected from the SIS18 accelerator which in turn is fed from the UNILAC linear accelerator. Once injected into the ESR ions can be stored up to several hours depending on the isotope, charge state and lifetime. They can be stored in bunches containing up to $1 \times 10^8$ particles. The experimental storage ring was designed to store almost every ion species in a wide range of energies [14]. The velocity can thus be chosen to specific values meeting for example conditions for laser spectroscopy measurements.

Not only the excitation wavelength is shifted, the photons emitted in forward direction also experience a blue shift to wavelengths down to 7 nm in the rest frame of the detector. According to [11] approximately 10 % of the initial ions are in the metastable state of which in resonance 50 % will be excited to the $^3P_1$ state by the laser. By tuning the excitation wavelength of the laser the wavelength of the resonance can be investigated.

# 3 Theory

This chapter will deal with the theoretical foundation of the processes relevant for the detection system. On the one hand this will be the relativistic processes of moving photon emitters and on the other hand a discussion about the production of electrons from solids caused by the irradiation with XUV photons.

## 3.1 Lorentz transformation

The behavior and movement of ions at high velocities, for example in particle accelerators, have to be treated relativistically. The changes in lengths and time is described by the theory of relativity from which certain transformation rules can be extracted. This includes the blue or redshift of wavelengths by the Doppler effect as well as the emission characteristics of relativistic ions. As stated in chapter 2 the wavelength shift for particles at relativistic velocities plays a crucial role to access the excitation wavelength of the ions. Therefore, the Doppler effect will be introduced in this section first. Afterwards the discussion extends to the photon emission distribution which shape is highly dependent on the velocity of the ion and will be of major importance for the collection of the photons and thus the detector design.

The transformation from the co-moving ion system to the rest-frame of the detector is done by the relativistic Lorentz transformation. The transformation rules are applied to four-vectors of the Minkovski space. Considering a particle with a certain velocity $v_x$ in the $x$-direction and the corresponding four-vector $\vec{X} = (x, y, z, ct)$, the components of the vector then transform in the following way:

$$\begin{aligned} x' &= \gamma(x - \beta ct) && (1) \\ y' &= y \\ z' &= z \\ ct' &= \gamma(ct - \beta x) && (2) \end{aligned}$$

The primed variables denote those of the moving frame and the non-primed ones those of the rest frame. The variables $\beta$ and $\gamma$ can be calculated via the equations

$$\begin{aligned} \beta &= \frac{v_x}{c} \\ \gamma &= \frac{1}{\sqrt{1-\beta^2}}. \end{aligned}$$

The Doppler effect even appears without relativistic treatment, so, when leaving relativistic effects aside, the wavelength shift can be calculated via the formula

$$\lambda = cT - v_x T \cdot \cos(\theta) \tag{3}$$

with the period $T$ of the emitter and an additional $\cos(\theta)$ term. The angle $\theta$ denotes the observation angle with respect to the direction of the movement of the light source. To include relativistic effects, the time dilation $t' = \gamma t$ can be implemented in the formula to derive

$$\begin{aligned} \lambda &= c_0 \gamma T' - v_x \gamma T' \cdot \cos(\theta) \\ \lambda &= c_0 \gamma \frac{\lambda'}{c_0} - \beta c_0 \gamma \frac{\lambda'}{c_0} \cdot \cos(\theta) \\ \lambda &= \gamma \lambda' (1 - \beta \cos(\theta)). \end{aligned} \tag{4}$$

To convert the expression to the energy shift of the photons, equation 4 can be altered by replacing the wavelength $\lambda$ with photon energy $E = \frac{hc}{\lambda}$. This results in

$$E = \frac{E'}{\gamma(1 - \beta \cos(\theta))}. \tag{5}$$

Figure 3 shows the angular dependency of the wavelength for the relativistic Doppler effect. The wavelength in the co-moving system is chosen to be $\lambda_{\text{comove}} = 17\,\text{nm}$ and is marked by the horizontal line. The colored graph shows the blue shift for angles in the forward direction down to a wavelength of $\lambda_{\text{min}} \approx 7\,\text{nm}$ and the redshift to wavelengths of about 40 nm, respectively. For the calculated graph, values of $\beta = 0.69$ and $\gamma = 1.38$ were assumed. It can be seen, that due to the relativistic Doppler shift the region of red-shifted photons already starts for angles smaller that 90°, whereas this would be exactly at 90° in case of non-relativistic treatment. This can be retraced when setting $\theta = 90°$ in equation 3.

The emitted photons are not only shifted in wavelength, they are also seen by the observer under a different angle. This again can be calculated via the Lorentz transformation. The angles can be expressed via

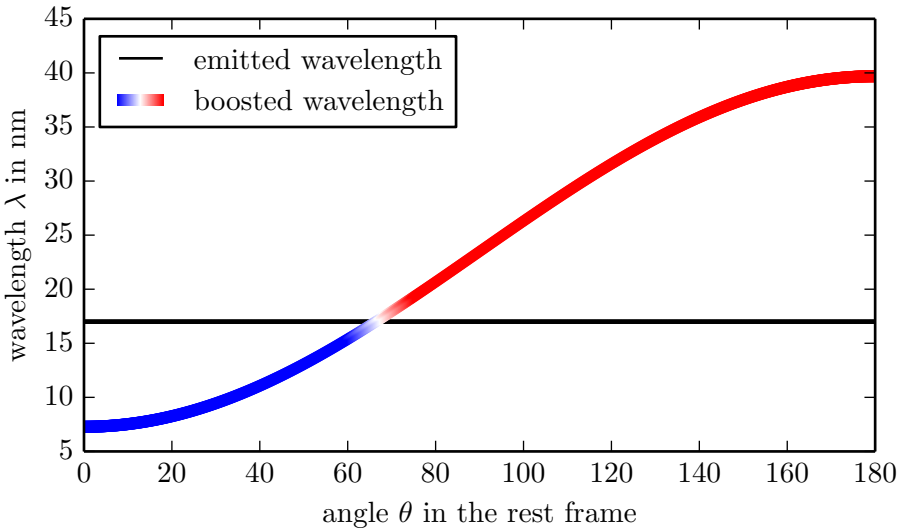


**Figure 3:** Wavelength shift for different observation angles due to the relativistic Doppler effect. The colored graph is calculated for a photon wavelength of 17 nm in the co-moving system, indicated through the horizontal line, for values of $\beta = 0.69$ and $\gamma = 1.38$.

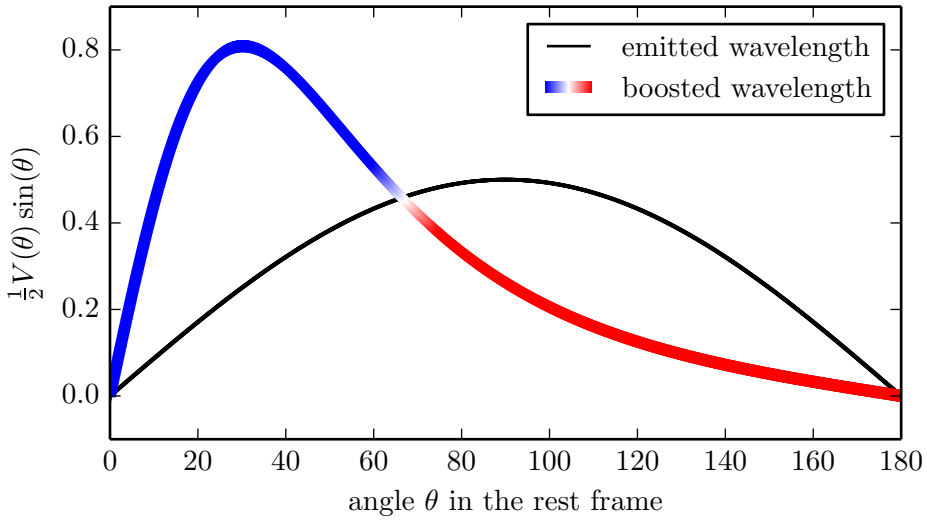


**Figure 4:** Angular distribution of the photons for a velocity of $\beta = 0.69$. The plot shows the distribution function $\frac{1}{2}V(\theta)\sin(\theta)$ from the integral expression in equation 9.

$$\cos(\theta) = \frac{x}{ct} \text{ and } \cos(\theta') = \frac{x'}{ct'}, \tag{6}$$

again assuming a movement along the $x$-axis. By applying equation 1 and 2 and substituting $x$, one can reach the result

$$\theta = \arccos\left(\frac{\cos(\theta') + \beta}{1 + \beta\cos(\theta')}\right). \tag{7}$$

To calculate the angular distribution of the photons one has to consider the ratio of the solid angles $\Omega' = \sin(\theta')\mathrm{d}\theta'\mathrm{d}\phi'$ and $\Omega = \sin(\theta)d\theta d\phi$. This value is denoted by $V$ and by the multiple use of equation 7 the final form

$$V(\theta) = \frac{1 - \beta^2}{(1 - \beta\cos(\theta))^2} \tag{8}$$

can be derived. The proportion of photons $P(\theta_1)$ emitted in a cone with half angle $\theta_1$ can be calculated via the integral

$$P(\theta_1) = \frac{1}{2}\int_{-\theta_1}^{\theta_1} V(\theta)\sin(\theta)\mathrm{d}\theta. \tag{9}$$

The distribution function $\frac{1}{2}V(\theta)\sin(\theta)$ in the integral is showed in figure 4 compared to the distribution of an emitter at rest. The factor $\sin(\theta)$ accounts for the decreasing volume element for angles approaching 0° or 180°. It becomes clear that most of the photons are emitted in forward direction.

## 3.2 Photoemission of secondary electrons

As it will become clear in the subsequent chapter, the emission of electrons from solid surfaces irradiated by photons plays a crucial role in the detector setup. Therefore, the processes from the penetration of the photon into the material to the emission of an electron from the surface will be discussed here. The fundamental process behind this is the photoelectric effect which describes the absorption of a photon under the emission of an electron from the inner shell of an atom. This primary electron travels to the surface, might produce secondary electrons on its path which then collectively escape from the material. The discussion in this chapter will focus on the emission characteristics of materials which are irradiated by photons in the XUV oder X-ray region.

Figure 5 shows a typical electron spectrum of a solid irradiated by XUV photons. It can

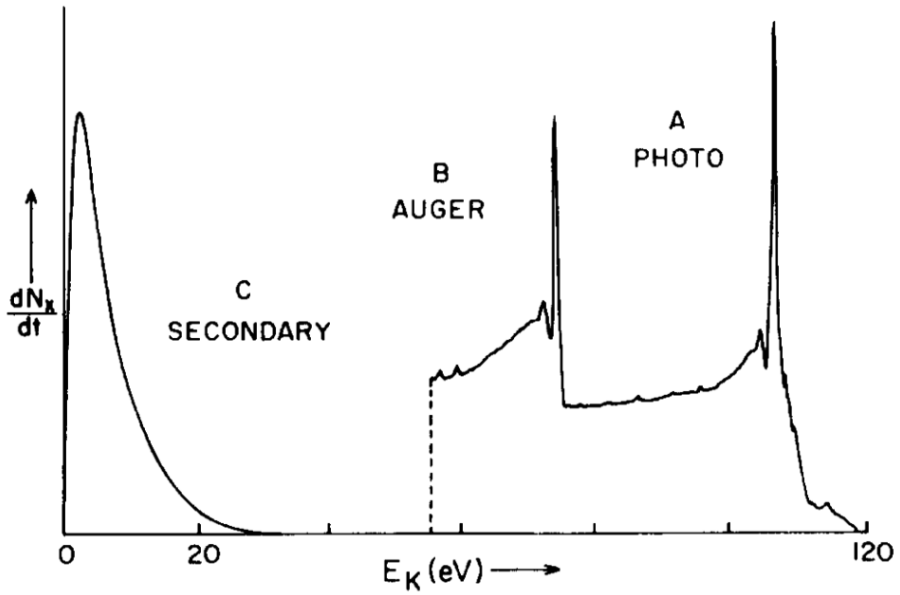


**Figure 5:** A typical electron energy distribution from a XUV excited solid. The left peak shows the low energetic secondary electrons whereas the right side shows the auger and primary photoelectron peaks which make out only few percent from the whole distribution and are scaled for a better visibility [15].

be separated in two regions containing the secondary electron spectrum at the low energetic part of the distribution and high energetic elastically scattered primary electrons which give rise to certain peaks in the spectrum broadened to lower energies by inelastic scattering. The high energy part is scaled for better visibility since the secondary electron spectrum contains almost all the electrons and only a few percent of the whole spectrum arise from primary electrons [16].

The discussion will start with processes that take place in metal solids and will essentially follow the theoretical and experimental investigation by Henke *et al* [15]. The incident photon penetrating the material will at some point interact with an atom. At that point the photon still has most of its initial energy since the photoionization cross section is greatest for the innermost shells and thus the photon does not loose energy through different interactions before. It is absorbed and transfers its energy to an electron from an inner shell ionizing the atom. Additionally to the primary electron, the atom might emit auger electrons in the process of de-excitation. Some of these "primaries" might reach the surface and escape the material without or with little loss of energy resulting in the high energetic part of the spectrum shown in figure 5. At this point it should be noted that

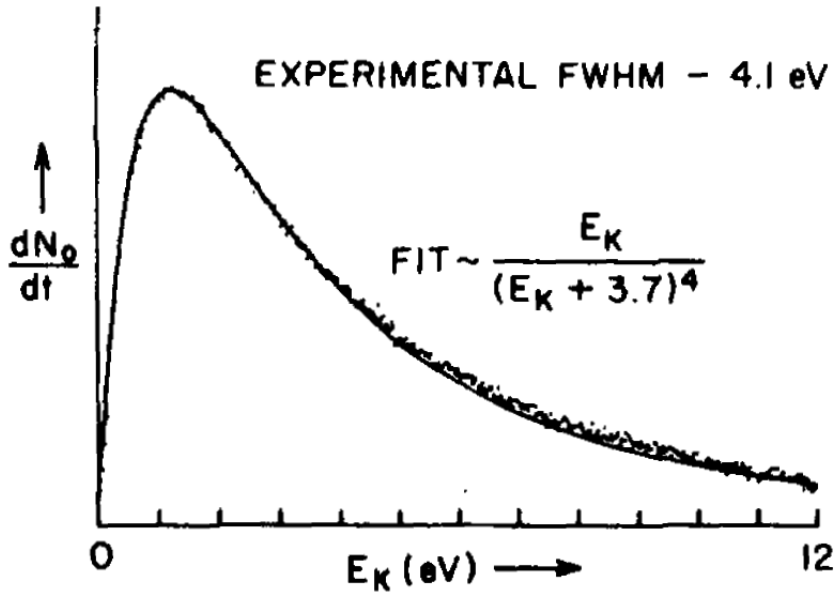


**Figure 6:** Secondary electron energy distribution from a gold cathode irradiated with 277 eV photons. The experimental data is fitted with the model that was stated in equation 10 under the assumption of a work function of $W = 3.7\,\text{eV}$ [15].

every electron has to overcome the work function $W$ to leave the material. This results in a certain threshold for electron emission from the surface by penetrating photons and also in an energy loss of $W$ for every emitted electron.

Some "primaries" may interact with loosely bound or conduction electrons which results in the production of other fast electrons or they might excite plasmons which then decay, resulting in the production of low energetic electrons. When the energy of the electrons decreases to values below 100 eV, electron-electron interactions with high momentum transfer lead to a cascade of low energetic secondary electrons. This electron cascade moves to the surface and leaves the material generating the low energetic part of the spectrum in figure 5. Following Henke *et al* the secondary energy spectrum can be derived via perturbation theory and mean free path analysis to

$$B = \frac{6W^2}{\pi} I_0 Y_0(E_0) \frac{E_K}{(E_K + W)^4}, \tag{10}$$

where $I_0$ is the intensity of the irradiating photon beam, $E_K$ is the electron energy above vacuum level, $W$ is the work function and $Y_0(E_0)$ denoted the total yield in terms of

electrons per photon. The total yield is given by

$$Y_0(E_0) = \frac{\pi ab\rho}{6W^2} \frac{E_0 \mu(E_0) f(E_0)}{\sin\varphi}. \tag{11}$$

Here $a$, $b$ and $\rho$ are material parameters whereas $\mu(E_0)$ and $f(E_0)$ denote the total mass photoionization cross section and the efficiency for energy conversion to secondary electrons, respectively, both depending on the photon energy $E_0$. Additionally, the $\sin\varphi$ term accounts for the angle of the incident photon with respect to the cathode surface. Figure 6 shows a measured secondary distribution of a gold cathode that is irradiated with a C-K$\alpha$-line at a photon energy of 277 eV. Equation 10 fitted to the experimental data is also shown in the figure.

Besides metals, a different work by Henke *et al* [17] discusses the secondary electron production for insulators. The processes leading to the secondary energy spectrum are different from the ones in metals and will be presented here on the basis of the stated work. The work function $W$ has to be replaced with the electron affinity $E_A$ which is defined as the difference between conduction band and vacuum level. The fundamental processes in the production of the primary electrons are the same, whereas the movement to the surface follows a different interaction. Here, the main process generating low energetic electrons are multiple-loss interactions between electrons and phonons resulting in a random walk to the surface. In this case it is assumed that the penetration depth of the incident photon is large compared to the mean free path for electron-phonon interactions giving rise to a huge number of these interactions. Again from quantum mechanical theories a secondary distribution function can be obtained:

$$\beta = \frac{4\pi E_0 \mu(E_0) f(E_0) \rho B}{2\pi} \frac{(\lambda_e \lambda_p)^{1/2}}{(1+\lambda_p/\lambda_e)^{1/2} + (\lambda_p/\lambda_e)^{1/2}} \frac{E_K}{(E_K + E_A)^3} \tag{12}$$

The distribution is similar to the one for metals. Here $\lambda_e$ and $\lambda_p$ denote the mean free path values for electron-electron scattering and electron-phonon scattering, respectively. The shape of the distribution is proportional to $E_K^{-3}$ which differs from $E_K^{-4}$ in equation 10 for metals. It originates from the different interactions of the secondary electrons on their way to the surface. In case of insulators it has to be noted that the electrons have to overcome the bad gap $E_G$ in order to reach the conduction band and finally leave the material. Figure 7 shows the secondary energy spectrum as it was measured with a AL-K$\alpha$-line at a photon energy of 1487 eV as well as a fit with the model stated in equation 12.

The spectrum clearly shows that most of the electrons leave the material with energies

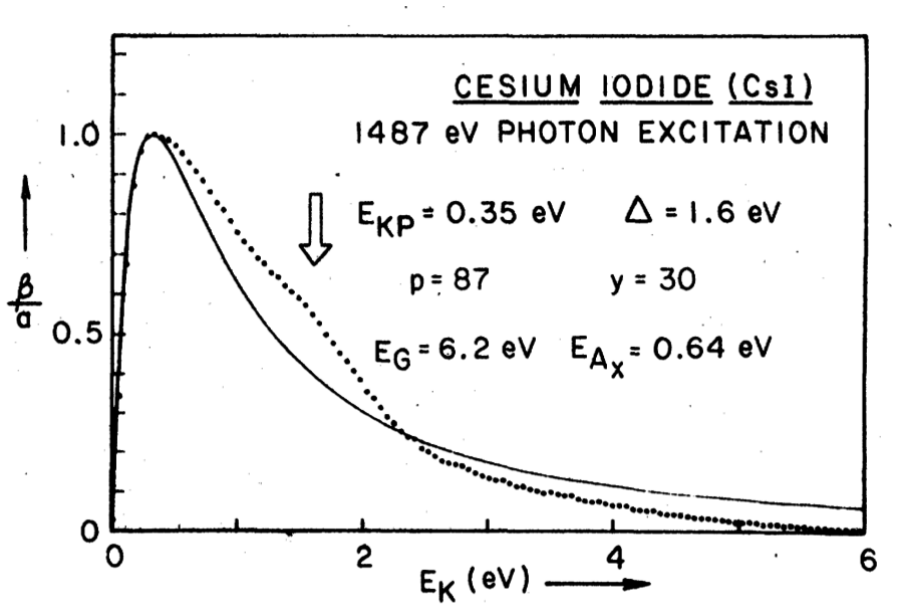


**Figure 7:** Measured secondary electron distribution of a 300 nm thick layer of the insulator caesium iodide coated onto a gold cathode. Data by Henke *et al* [17] with a AL-K$\alpha$-line source at a photon energy of 1487 eV. Experimental data is compared to a fit of the model stated in equation 12.

close to zero. The tail of the spectrum goes up to a maximum of 6 eV. This is in contrast to the electron distribution from metal surfaces. The peak position is higher and also the distribution is broader, which clearly shows that the drift process in insulators concentrates more electrons at lower energies. In between, indicated by the arrow, there is a small bump in the spectrum which, according to [17], can be denoted to plasmon de-excitations. From experimental data it is observed that the shape of the secondary energy distribution is nearly the same for different photon excitation energies [16].

Besides the similar shape of the distribution, the stated articles show a huge difference in the total electron yield between metals and insulators. These results indicate an electron yield which is one to two orders of magnitude higher for insulators in the UV or XUV photon region. Especially at wavelengths of photons in the XUV region metals show yields of about only a few percent in terms of electrons per photon. Figure 8 shows graphs for typical metals such as tungsten or aluminum for excitation wavelengths in the range from 5 nm to about 100 nm. The electron yield is very low at short wavelengths and rises to about 15 % at higher wavelengths. The shape of the two examples is typical for many metal substrates. In comparison, a work by A. Breskin [19] showed the electron yield

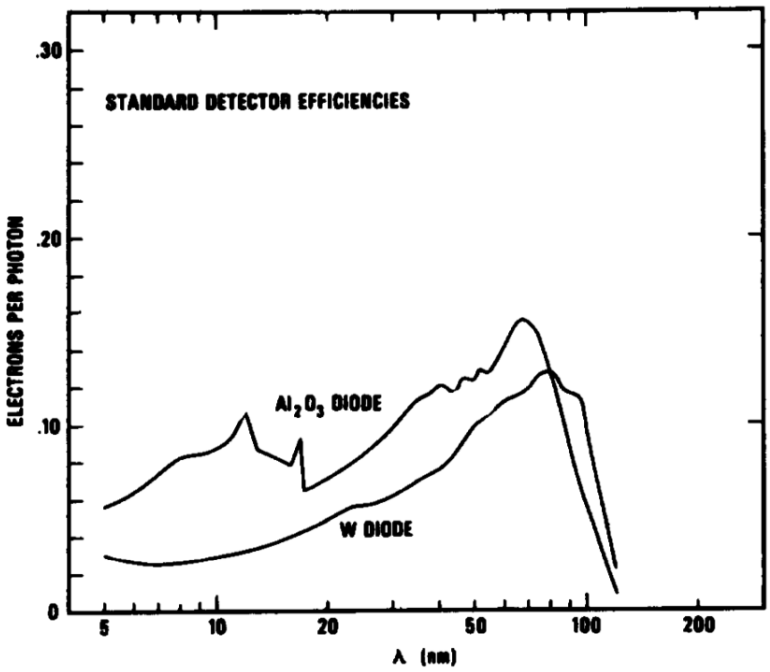


**Figure 8:** Electron yield from typical metal substrates illuminated at excitation wavelengths in the range of a few nanometers up to 100 nm. Curves are shown for oxidized aluminum and tungsten taken from [18] showing electron yields of about a few percent for wavelengths in the XUV region.

for different insulators for excitation wavelengths from 90 nm to about 160 nm. This is displayed in the left graph in figure 9. One can see electron yields up to 70 % for various insulators. What can also be taken from the graph is the fact that caesium iodide has the highest yield in the stated region. This is emphasized by the graph on the right side of figure 9 shows a comparison of the yield of caesium iodide and copper iodide with aluminum for wavelengths of 5 nm to 50 nm [18]. Here both materials are vacuum evaporated onto aluminum substrates with a layer thickness of about 300 nm. The striking peak at a wavelength of 11 nm can be assigned to a photo absorption peak in atomic caesium produced by the photo ionization of the 4d electrons.

The electron yield enhancement in insulators over the whole wavelength region can be attributed to the electron-phonon scattering process which enables high escape probabilities for electrons created deeper in the material, since the energy loss per interaction is very low. For most of the insulators the electron affinity is very low, enabling an easier escape from the surface to the vacuum compared to metals. As caesium iodide has a very

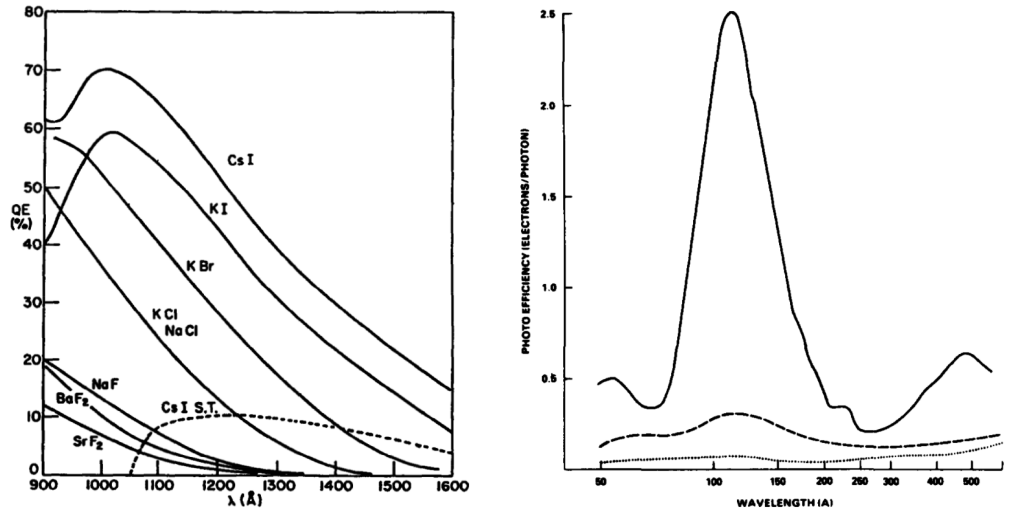


**Figure 9:** Left: comparison of the quantum efficiency for different alkali halides taken from [19] in the UV wavelength region; right: comparison of the yield of 300 nm thick layers of caesium iodide and copper iodide coatings with a pure aluminum cathode in the XUV wavelength region taken from [18].

low electron affinity of $E_A \approx 0.2\,\mathrm{eV}$, it is currently the material with the highest known electron yield in the UV wavelength region [19]. Important for all the insulators is a certain cut-off wavelength which depends on the height of the bad gap. Thereby no electron emission can be observed for photon energies below this threshold.

# 4 XUV detector setup

This chapter will outline the detection principle which is applied to detect the emitted photons, the therefore designed detector with all the components and features as well as the experimental setup in the laboratory in Münster. The chapter will close with a short discussion of possible improvements on the old detector setup, as it is the main topic of this thesis to develop a final optimized detector setup.

## 4.1 Detection principle

As already introduced in section 3.1, photons emitted by moving particles at relativistic velocities are mainly directed into a narrow forward cone. To collect these photons, a cathode plate with a central slit is brought into the beam line. Figure 10 pictures a scheme of the detection process where the emitted photons from the laser-excited ions hit the plate. The slit allows the ions to pass while covering most of the area around and thus collecting a great fraction of the emitted photons. Since the photons in this experiment have wavelengths in the XUV region, they cannot be collected or reflected with optical components, instead they penetrate the plate and thus produce electrons via the photoelectric effect. These primary electrons create secondary electrons which leave the plate as low energetic secondary electrons (compare section 3.2). These electrons are then guided electromagnetically from the surface out of the beam line onto a detector.

Since the ion bunch has to be cooled and focused before the plate can be brought into the beam line, the cathode plate is mounted to a carrier which can be moved in and out of the beam line via a linear feedthrough. This technique has successfully been used in the LIBELLE experiment, where a parabolic copper plate with a central slit was used to reflect emitted photons onto a photomultiplier [12].

## 4.2 Previous detector setup

The focus of this work is to improve certain aspects of an already existing setup. Therefore, the old detector setup will be presented in detail before introducing possible improvements. For a detailed description of the manufacturing process and the ideas that lead to the old detector design, it is referred to the doctoral thesis of Jonas Vollbrecht [20]. A picture of the assembled detector with all its components is presented in figure 11.

The previously mentioned cathode plate, which is one of the central units of the detector, is mounted at the very end of a carrier. The plate itself has a diameter of 156 mm and is mounted at an angle of 120° with respect to the carrier resulting in an angle of 30° with

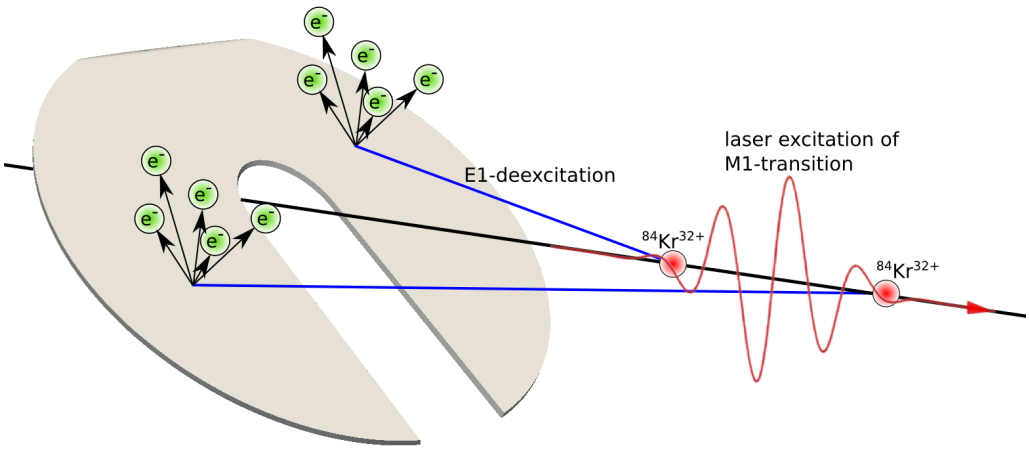


**Figure 10:** Schematic picture of the detection principle showing the krypton ions which are excited by the anti-collinear arranged laser. The emitted photons during de-excitation hit a cathode plate and generate mostly secondary electrons on the surface, which are guided out of the beam line onto a detector.

respect to the direction of the ion beam. The slit has a width of 30 mm which opens the path for more than $3\sigma$ of the ions. In the work of Denis Anielski [21], the radial extend of the ion beam at ESR is discussed in detail.

A ring-shaped electrode is mounted directly above the cathode plate also orientated with the same angle as the plate. Close by there are three additional ringlike electrodes mounted to the carrier. The cathode plate together with the first ring electrode, but also the three other rings can be supplied with voltages via a BNC feedthrough at the top of the detector. Through a negative voltage applied to the cathode plate the electrons that are produced on the surface can be accelerated away from the plate and thus out of the beam. They are then guided onto a detector unit. Here it becomes clear that the angle of the cathode plate is a trade-off between potential target size for the photons and the flight direction of the produced electrons, which are accelerated perpendicular to the cathode surface. The potentials at the three ring electrodes may be used for a finetuning of the flight paths via electrostatic guiding. These stated components are movable via the carrier which is connected to the linear feedthrough. It can be moved in and out of the beam line via a pressured air motor. A vernier adjustment of the whole carrier can be conducted with a two axis table connected through a vacuum bellow. Besides the different potentials which can be applied to all the electrodes, the carrier and also the MCP shielding are electrically

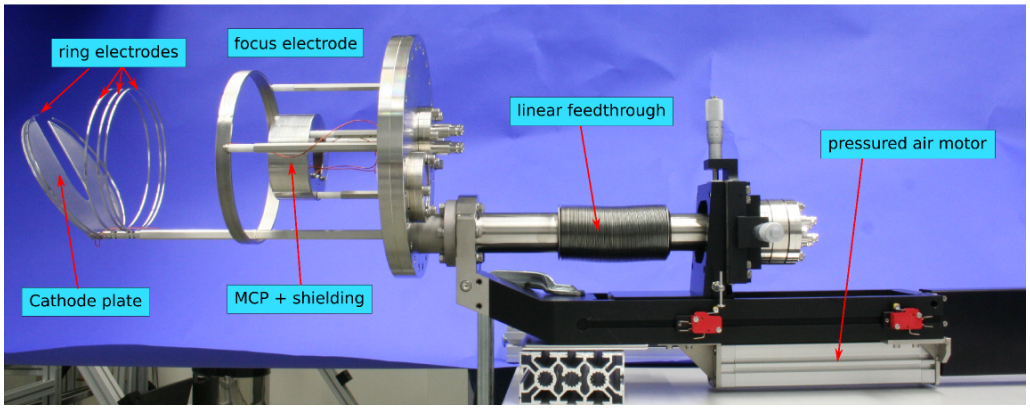


**Figure 11:** Old detector setup with all the components (from left to right): cathode plate, ring electrodes, focus electrode, microchannel plate detector, mounting flange, linear feedthrough and pressured air motor. Solenoid coils are mounted outside the vacuum and not shown in this picture.

separated and lay on grounded potential.

Apart from the movable parts of the detector, there are two high voltage components which are fixed directly to the CF200 flange. This is on the one hand another ring-shaped electrode to focus the electrons passing by and on the other hand the detector itself which consists of a microchannel plate detector (MCP) from RoentDek [22]. These components can be connected to high voltage supplies via SHV feedthroughs. The MCP is integrated into a cylinder like shielding and has an active diameter of 40 mm.

The basic principle of a microchannel plate is similar to that of a photomultiplier in multiplying single electrons in an electron cascade. The idea is to enhance a weak signal by many orders of magnitude and pick up the electric signal which is generated by the cascade electrons. A schematic view of a microchannel plate is shown in figure 12. The plate consists of small holes, which are covered with a semiconductor material. When a particle, i.e, an electron or photon hits the semiconductor surface it produces electrons that drift through the channel via a strong electric potential. Along their flight paths they produce a lot of secondary electrons through interactions with the semiconductor walls, resulting in an enhancement of the signal by a factor of up to $1 \times 10^7$.

The electron cascade is detected via a voltage drop on an anode that is placed behind the microchannel plate. Figure 13 shows a scheme of the MCP as it is assembled and integrated into the MCP shielding. It shows two microchannel plates stacked together

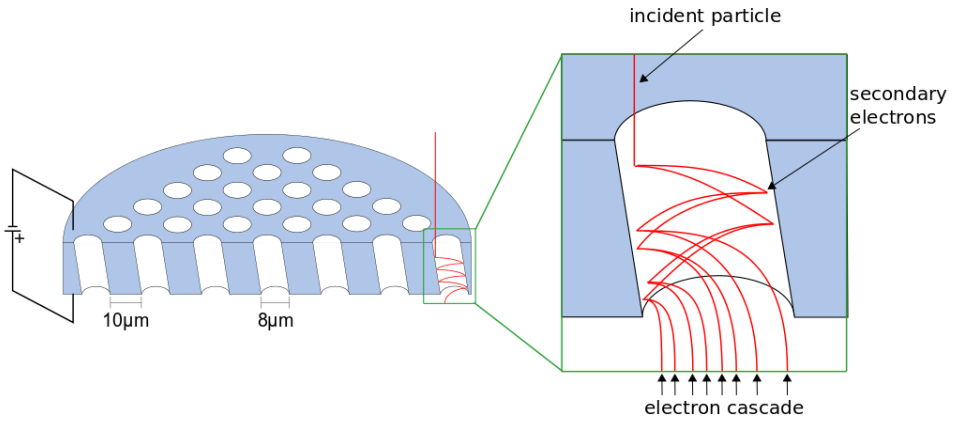


**Figure 12:** Schematic view of a micro channel plate with an enlarged inset indicating the basic working principle. The incident particle launches an electron cascade in the microchannel which leaves the channel as an enhanced and detectable signal [23].

with a timing anode placed behind them. The two channel plates are stacked in a chevron configuration, where two identical channel plates, in which one is rotated about 180°, are placed directly on top of each other. This reduces ion feedback inside the device significantly.

As microchannel plates are operated at drift voltages in the region of a few keV, they have to be operated in high vacuum conditions to prevent sparkovers from surface contaminations. Since the detector shall be used in an experiment at ESR, it is constructed for the usage in high vacuum conditions and thus all components are certified for ultra high vacuum below pressures of $1 \times 10^{-10}$ mbar.

In the course of the initial detector development it became clear that the electrons cannot be guided from the plate to the MCP detector only by using an electric field shaped by the ring electrodes. To achieve a proper guiding, a coil system is installed outside the vacuum which produces a magnetic field over the whole detector. In this case an old two-coil system was used which consists of two solenoid coils connected to each other. The system can be mounted at the CF200 flange. Figure 14 shows a picture of the coil system. To get an impression of the general course of the field lines it is referred to the work of Jonas Vollbrecht [20].

On top of the CF200 flange there is a CF35 flange which is not substantial for the de-

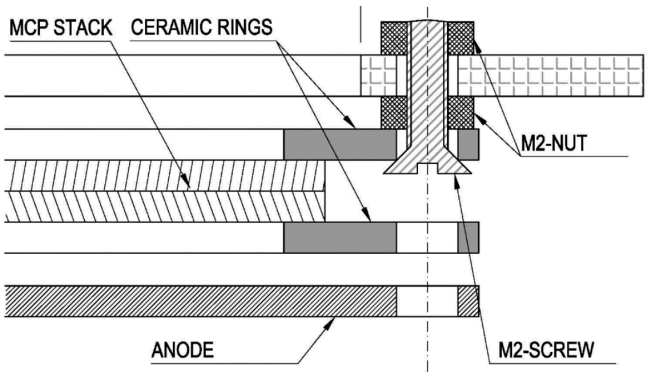


**Figure 13:** Schematic view of the assembled microchannel plate taken from [22]. Two microchannel plates are stacked in chevron configuration and fixed between ceramic rings. The anode is places behind the channel plates to pick up the signal.

tector functionality. It can either be used for a small vacuum window or another BNC feedthrough which is used when operating with an UV-LED inside the vacuum. The LED was used for certain measurements and is further described in section 6.1.

## 4.3 Laboratory Setup

This section builds on the previous section, introducing the whole setup in the laboratory in Münster including the power supplies and the readout electronics. The detector was integrated into a new vacuum chamber specifically designed for the detector. It consists of a rotatable CF200 flange at the top where the detector is attached. In figure 15 the whole setup in the vacuum chamber and the solenoid coil system is displayed. The vacuum chamber also has two CF100 flanges at the sides where one is used for a vacuum pump and the other one for a glass window.

The vacuum pump is a turbo pump of the model HiPace300 from Pfeiffer Vacuum achieving vacuum conditions in the displayed chamber in the order of $1 \times 10^{-9}$ mbar without baking out the chamber. To produce the desired prevacuum a diaphragm pump is connected via the turbo pump to the chamber. At the front there is a vacuum gauge device mounted at a CF18 flange to measure the vacuum conditions in the chamber. The opening at the bottom of the chamber is closed with a CF200 blind flange. The solenoid coil system that is mounted around the tube for the generation of the magnetic field is also shown in the picture. The chamber was designed such that the cathode plate is placed exactly in

**Figure 14:** Picture of the solenoid coil system which was used in the lab experiments. The coils fit around the setup and can be attached to the mounting flange. It consists of two magnet pairs from which the outer and bigger coils were used in this thesis to create the magnetic field.

front of the window and additionally the detector was rotated via the top flange such that the cathode plate directly points towards the window. By that, photon sources can be placed in front of the window to illuminate the plate. The detector shown is fully operational connected to all the voltage supplies via BNC or SHV cables. Most of the modules for the voltage supply and the readout process are integrated into a NIM crate. Solely the power supply for the solenoid coils comes from an external device. Figure 16 shows the NIM crate with all the essential modules. The right side contains a ISEG NHQ 224M high voltage module which served as the supply for the three MCP plates. The module creates the two voltage outputs for the front plate and the anode plate and through a voltage distribution module the difference of these two can be connected to the back plate. All three voltages were provided with SHV cables and connected through the corresponding feedthrough adapters to the plates. Via a small readout circuit, which can be seen as the small metal boxes (compare figure 15), the signal from the MCP can be coupled out and connected via BNC cables to the readout modules.

As a second supply, a Canberra 3102D high voltage module served as the source for the focus electrode. It was also connected via a SHV cable to the SHV feedthrough adapter. The third supply is a low voltage MHV-4 module by mesytec which provides voltages for the movable parts of the detector consisting of the cathode plate and the ring electrodes.

All voltage outputs were connected via the BNC feedthrough adapters to the corresponding component. Additional to the NIM components there was the already mentioned power supply for the solenoid coil system. This device (model EA-PS 3032-05B by Elektro-Automatik) creates currents up to a maximum of 5 A. Both coils were connected to one circuit provided by this power supply. In addition to the voltage supplies, the readout modules are places on the left side inside the NIM crate. The readout process takes place in four steps, processing the signal from the raw MCP signal to a logic rectangular pulse. The first module is a 16 channel fast amplifier (Caen Model N979) which takes the MCP signal from the anode and scales it by a factor of 100. Therefore, the signal is enhanced twice, since every channel amplifies the input by a factor of 10. The output signal of the backplate or frontplate of the MCP can be displayed with an oscilloscope when requested. The enhanced signal passes through a discriminator (Caen Model N840). At a certain threshold the module produces a logic signal with an adjustable width. Both can be adjusted and are optimized in the given setup to parameters of width = 3 and thres = 125. Figure 17 displays a schematic overview of the signal

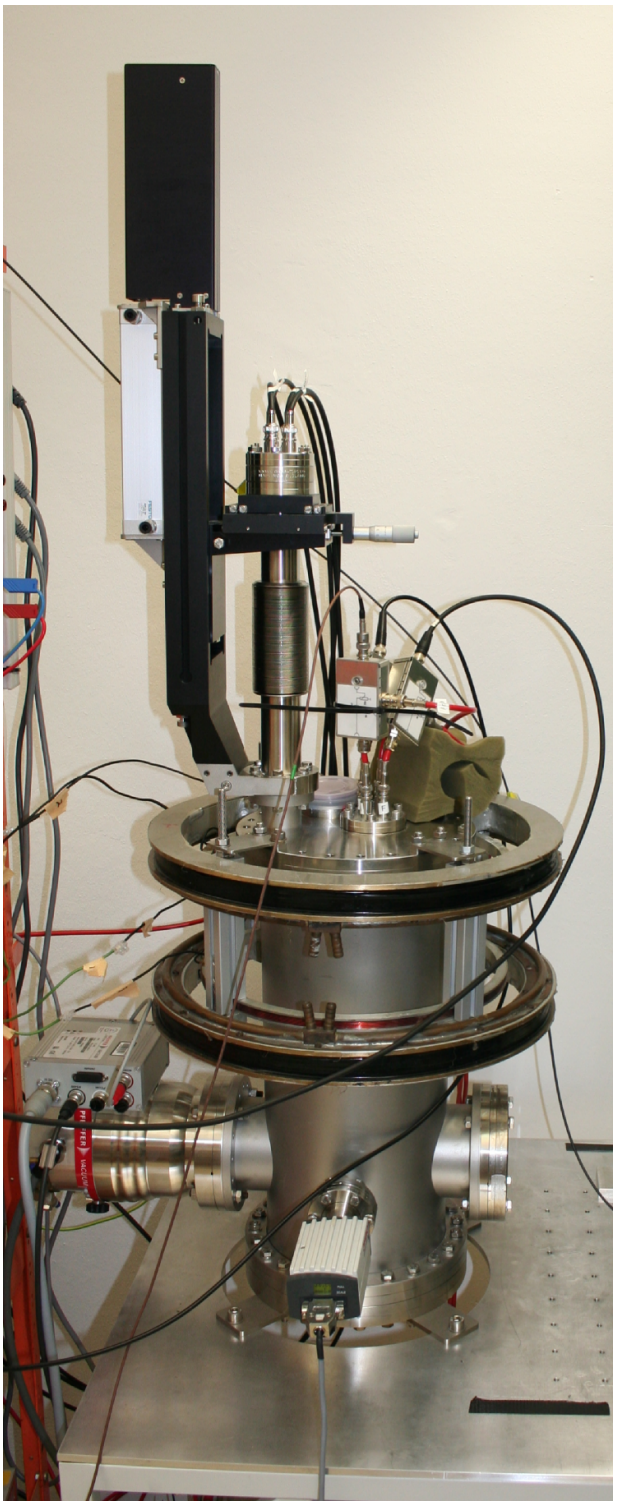

**Figure 15:** Detector setup as it was installed in the laboratory in Münster.

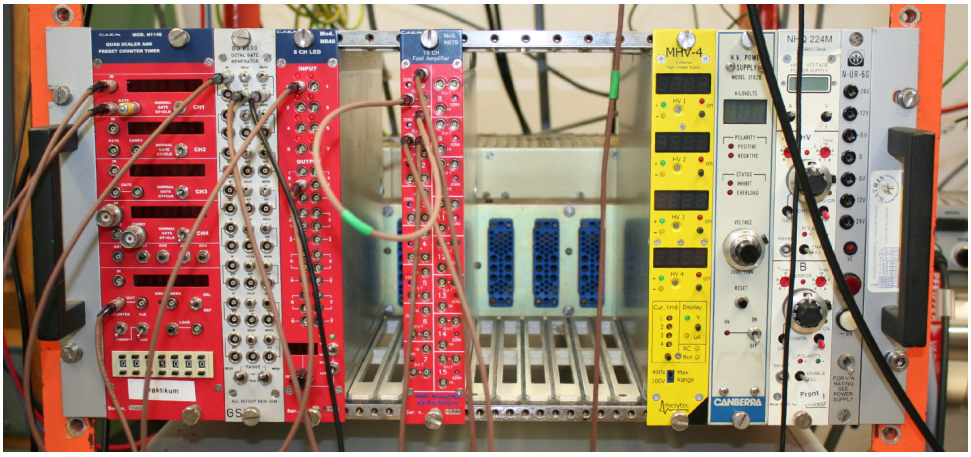


**Figure 16:** NIM crate with the voltage supply modules for the detector parts and the readout electronics for the signal processing of the MCP signals. Modules from left to right: counter, gate generator, discriminator, amplifier, electrode voltage supply, focus electrode supply, MCP supply.

form during the process. As the signal from the MCP shows a post-pulse oscillation, it would be treated as two counts after the discriminator. To treat both signal as one event a Gate and Delay Generator Model GG 8000 was used. It produces a logic signal with a certain adjustable width and delay. The gate was chosen experimentally to a width of 200 ns to cover both pulses from the discriminator. Finally, the signal was counted by a Caen Model N1145 Quad Scaler and Preset Counter Timer, which counts all events in a tunable time window.

## 4.4 Possible improvements

The previous section introduced the experimental surroundings and the detector state at the beginning of this thesis. This section will now present certain aspects of the detector with open potential for further optimization. There are mainly three aspects which can be significantly improved. The first is the cathode plate, as the size and angle can be changed to enhance the collection efficiency. Intuitively a steeper angle results in a higher effective target for the photons, but since the produced electrons are accelerated perpendicular to the surface via a repelling potential the guiding properties will suffer under a steeper cathode angle. The incident angle under which the photons hit the cathode is also important since it is a crucial input variable for the electron yield (compare equation 11). Through a simulation of different angles the optimal configuration between these aspects can be found. After finding the right angle, the size of the plate can be maximized under

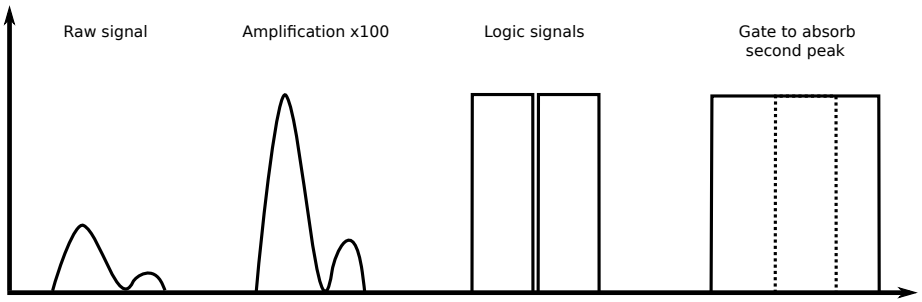


**Figure 17:** Scheme of the readout steps with indications for the shape of the signal after passing through every single modules. The raw signal from the MCP is transformed into a countable logic signal.

the restriction of the physical dimensions of the vacuum pipe at ESR. This optimization process is described in detail in section 7.1.

A significant enhancement of the electromagnetic guiding of the detector can be achieved by a completely new coil setup. The coils shown in figure 14 are not adjusted to the requirements of the detector. A system creating a magnetic field which is tightly focused at the MCP, but widely opens at the cathode plate to collect and focus as many electrons as possible onto the detector. The magnetic field created by the old system is nearly homogeneous, covering only a very small area of the cathode plate and thus imaging only a small fraction of the electrons from the surface to the MCP detector. This optimization process was carried out after the angle and shape of the cathode plate was fixed, otherwise there would be too many open parameters to evaluate, namely the shape of the cathode plate, the coil parameters such as radius, position and current as well as the electrode potentials. The development of a new coil design will be presented in section 7.2.

The last part that can be optimized is the electron yield of the cathode plate. There are several works that deal with semiconductor or insulator coatings on metal surfaces. Most of the works introduce caesium iodide as a suitable coating for an enhanced electron yield in the XUV wavelength region of this experiment (compare section 3.2). Following that idea, this work will evaluate the effect of a thin layer of caesium iodide coated onto the cathode plate through measurements with small probes. The results from this investigation and their implications will be discussed in section 7.4.

In the course of the optimization process of the detector there were also significant changes

in the simulations. The old simplified model will be replaced by a detailed version taken from the technical CAD drawing of the detector. New and more precise modelings of the physical effect will be implemented to better understand the behavior of the detector and to be able to reproduce the experimental results. This will be the foundation for reliable predictions concerning the optimization process of the cathode plate and also the solenoid coil system. This work is therefore split in two major parts separating the development of the simulations with the old detector setup and the corresponding measurements from the optimization process and the investigation of the features of the newly developed setup.

# 5 Simulations

This chapter will introduce the development of the simulation program including a short introduction to the SIMION simulation package, the implementation of the detector geometry as well as the set up of the complete simulation program with all the relevant processes.

## 5.1 SIMION 8.1

SIMION is a simulation program which was developed by Don C. McGilvery at Latrobe University in the late 1970s [24]. It was later adapted to personal computers by David A. Dahl at the Idaho National Engineering and Environmental Laboratory. It is based on the Windows platform, but can be adapted on Linux systems via Wine [25]. SIMION is specialized in the calculation of ion trajectories in electric and magnetic fields. It is possible to develop static electric and magnetic potentials via different geometries which can be implemented into the project. It is also possible to generate solenoid coils which can be implemented via a user program. For every electric or magnetic source the fields are calculated via the Laplace equation

$$\Delta V = 0 \tag{13}$$

and the Biot-Savart law

$$\vec{B}(\vec{r}) = \frac{\mu_0}{4\pi} \int I \frac{\vec{r}}{|r|^3} \mathrm{d}\vec{l}. \tag{14}$$

Then all electric or magnetic fields are superposed in certain points on a three dimensional grid serving as the basis for the trajectory calculations. It is possible to develop own models via geometry files but also to import StereoLithography (.stl) files, i.e., technical drawings or models developed by 3D modeling software. The voltages can then be set for every potential source separately. One can create different particles by defining a set of parameters, i.e, charge and mass. Additionally, every particle gets a certain start position and momentum vector. After setting all the necessary initial parameters, SIMION calculates the step by step ion trajectory. The magnetic and electric field components from the pre-calculated grid are therefore evaluated together with the parameters of the particle at the current position. This is calculated via the Lorentz force equation

$$\vec{F} = q\left(\vec{E} + \vec{v} \times \vec{B}\right). \tag{15}$$

The step will be repeated in a certain time step interval until the particle hits an electrode

or leaves the pre-defined volume. The whole simulation is controlled via a LUA based user-program which communicates with the field or trajectory program section via a set of predefined variables. Here the user is free to create, delete or manipulate every particle the desired way during the simulation, but can also track and calculate ion positions or velocities if requested.

In the course of this thesis, a new CAD based geometry together with a newly developed user program was implemented into SIMION. The following sections will be about the implementation and afterwards discuss the properties and processes that are included in the simulation through the user program.

## 5.2 Implementation of the new model

This paragraph describes how the models was integrated in SIMION and what parts of it took an important role. Due to the fact that many of the simulations were run at times when the final setup was not developed, the simulations were run with a constantly changing detector setup. To get a first impression how an imported model looks like in SIMION, figure 18 shows two versions of the old detector setup as it was the starting point for this thesis. On the left side it shows the model which was developed with the SIMION geometry tools and on the right the implemented version from the technical CAD drawing. This section will only deal with the basic implementation process in SIMION and will not go into a detailed description of the program features. Since SIMION can only apply voltages to different separately imported geometry files, every object to which a certain voltage will be applied has to be implemented on its own. In this case this makes up to ten imported models which are in total the cathode plate, the cathode electrode, the three separately mounted ring electrodes, the focus electrode, the three MCP plates and finally the surrounding tube. The tube was not implemented in the old geometry, but served as a representation for the vacuum chamber around the detector (see experimental setup in section 4.3). The tube is not shown in figure 18 to open the view for the detector components. Additionally, an empty grid for the magnetic field was implemented to predefine a certain volume in which the magnetic field from the coils is evaluated. There was no need to implement the coil as a magnetic source geometry, because it was possible to construct a hypothetic coil with the user program.

For the first experiments this geometry was sufficient since it very well approximates the setup in the laboratory. Later it was necessary to simulate a huge part of the beam line to created the needed photon distribution on the cathode plate. Therefore, a completely separated second simulation was created which only includes the cathode plate as a target for

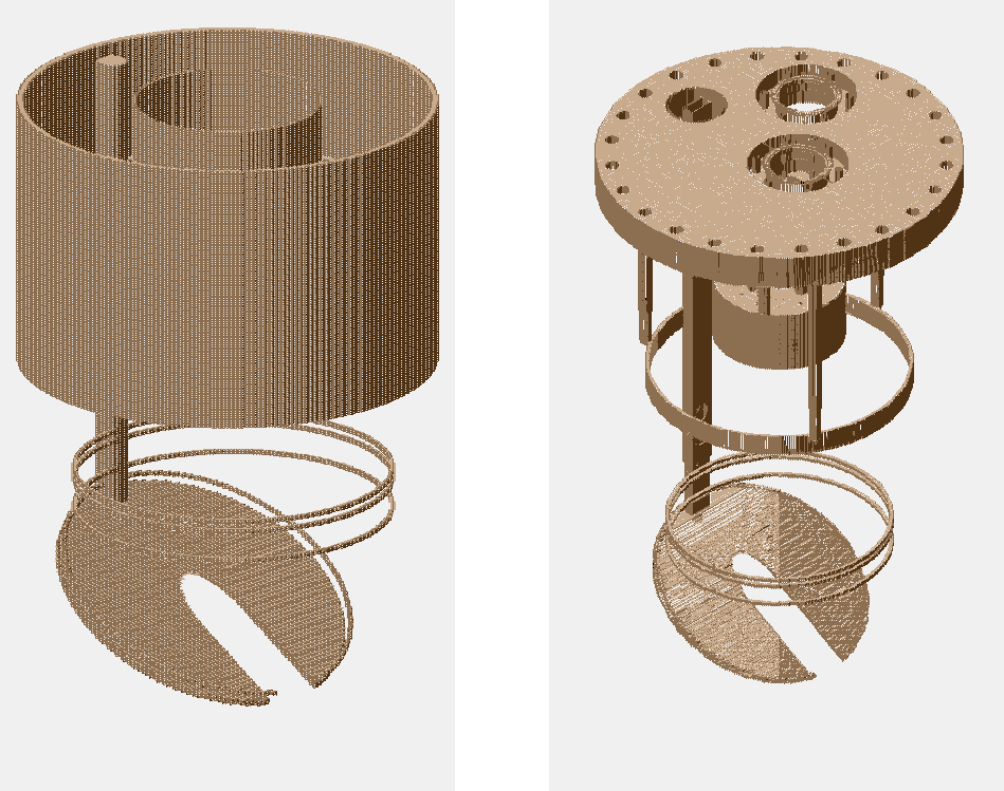

**Figure 18:** Comparison of the different SIMION models. Left: Old version which was developed with the SIMION geometry tools; right: New version of the detector from the technical CAD drawing with all tiny details of the actual geometry.

the emitted photons. Since SIMION always creates a rectangular box around the model, the grid would be too big for common computer memory to process, if parts of the beam line et cetera will also be included and thus both simulations could not be integrated into one.

After setting up the models in SIMION the user program was developed to create the photons emitted by the excited ions and the electrons from the cathode surface, calculate all the necessary parameters and finally save all the needed data from the simulation. The next section will explain in detail the physical processes that were implemented into the simulation.

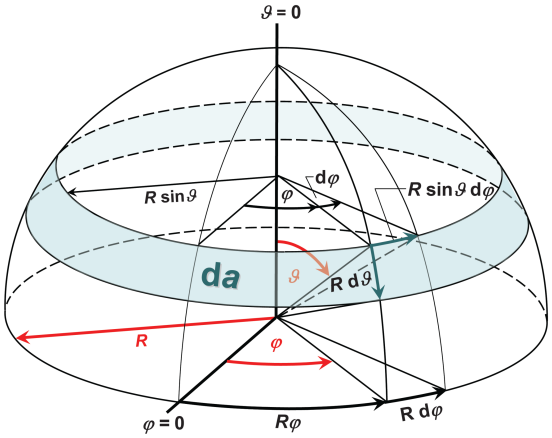


**Figure 19:** Dependency of the surface element d$a$ of the elevation angle $\vartheta$ [26]. The relation $\mathrm{d}a = R^2 \sin\vartheta \mathrm{d}\vartheta \mathrm{d}\varphi$ shows the necessity for the introduction of the $\sin\theta$ term which was already used in equation 9.

## 5.3 Implementation of physical processes

This chapter will deal with all the implemented physical effects and properties. These are for example the photon emission angle distribution from the excited ions which are emitted along the beam line or the energy spectrum of the electrons that leave the cathode as they were introduced in chapter 3. The discussion will involve the underlying understanding and modeling of these effects as well as the implementation steps in SIMION. The final simulation process will take place in two steps, so the discussion will first deal with the creation and behavior of the photons and in the second step with the production and guiding of the electrons.

The ions circle in the ESR with a velocity of 0.69 c, so the emitted photons are Lorentz boosted into a forward cone (compare section 3.1). Since the simulation is run in the rest frame of the detector, this distribution has to be reproduced in the simulation. This can be achieved in two steps. In the first step a uniform random angle distribution on a sphere is created for the co-moving ion frame. This represents the spherical photon emission from the ions. As a second step, equation 7 is used to transform all the random angles from the co-moving system in the rest frame of the detector. That will create exactly the given distribution displayed in figure 4.

In detail it is necessary to generate two random numbers. The first lies between 0 and $\pi$ as for the elevation angle $\vartheta$ and the second between 0 and $2\pi$ for the azimuth angle $\varphi$. The problem here is that in this case the angles will not be isotropically distributed around

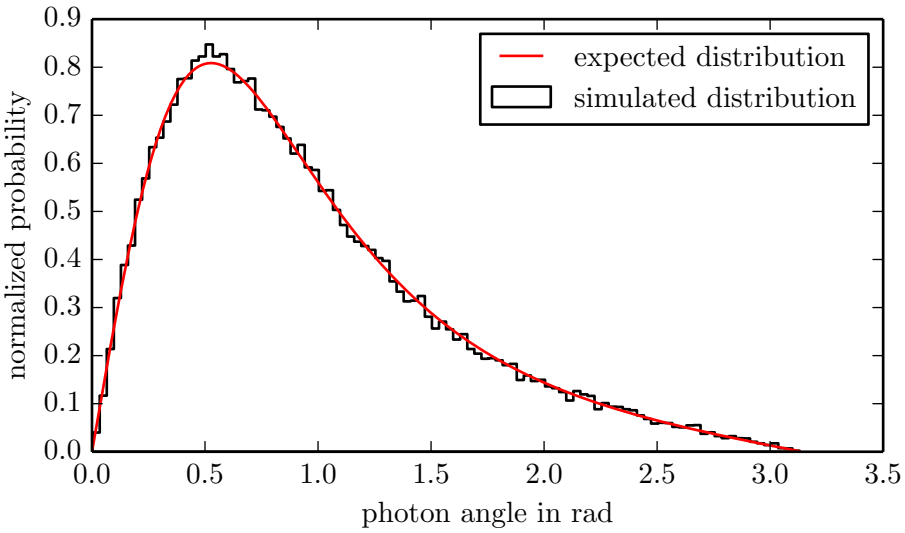


**Figure 20:** Graph of the expected angular distribution of the photons from figure 4 compared to a histogram from the simulated distribution by the creation of 60000 photons.

the sphere. It has to be taken into account that the surface element d$a$ changes with the elevation angle proportional to $\sin(\vartheta)$ which can be seen in figure 19. To compensate this effect the distribution is weighted with a factor of $\sin(\vartheta)$. The resulting distribution is displayed in figure 20 compared to the theoretical distribution shown from figure 4. For this graph 60000 photons were simulated and it can be seen that the histogram of the simulated distribution very well reproduces the expected distribution.

The photons from the ions will not be emitted from a specific point in front of the cathode plate, but will rather be emitted continuously over a certain distance. So one has to account for the moving particle bunch at ESR. Additional to the length of the emission line, the ion bunch has a certain radial extend. In the work of Denis Anielski [21] the extend of the ion beam at ESR is deeply discussed and a value for the standard deviation is given as $\sigma_{\text{beam}} = 2.5\,\text{mm}$ to $8\,\text{mm}$. The number and also the sort of ions in this experiment of this work are different compared to the stated work, therefore a medium value of $\sigma_{\text{beam}} = 4\,\text{mm}$ was approximated for the simulations. The realistic ion beam does not follow a Gaussian distribution, but it can be quite well approximated through a Gaussian distribution since minor deviations are already covered by the uncertainties in the extend of the ion beam. The distance over which photons will be created is more important for the collection efficiency of the plate.

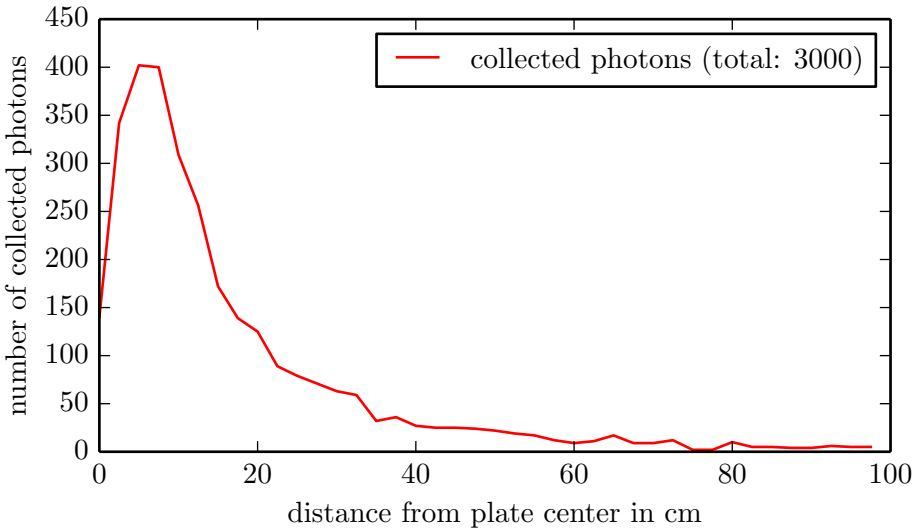


**Figure 21:** The graph shows the number of photons that hit the cathode plate from various distances from the center of the plate. The plotted data also indicates the range in which photons were generated for the simulation since a negligible amount of photons will be collected for distances greater than 1 m.

To investigate the collection behavior in dependence on the emission point along the beam line, photons were simulated for various start positions. The graph presented in figure 21 shows the ratio of collected photons to emitted photons depending on the distance to the cathode plate for 40 equidistant points starting in the center of the plate to a distance of 1 m. One can see a clear peak at small distances which takes shape because photons with high emission angles with respect to the beam line will be collected at small distances, but at higher distances only the photons with very small angles will be collected. Only about 1 % of the emitted photons will be collected from a distance of 1 m. In the paper by Danyal Winters [11] the bunch length is stated to be 15 m. It can be clearly seen that only a small fraction of the photons will be collected, namely those that will be very close to the cathode plate when de-exciting. As virtually no photons will be collected behind distances greater than 1 m a range from 0 cm to 100 cm with an interval of 2.5 cm were chosen as starting points for the simulations. The total amount of photons that hit the plate is 3000 from 60000 initial photons. This calculates to a ratio of 5 %.

The last implementation in the first part of the simulation was to account for the angle under which the photons hit the plate. As discussed in section 3.2 the electron yield $Y$

from the cathode plate depends on the angle of the incident photon with respect to the cathode surface and is proportional to

$$Y \propto \frac{1}{\sin(\varphi)}. \tag{16}$$

For every photon that hit the plate, the incident angle and though the enhancement factor $1/\sin(\varphi)$ is calculated. Since the point where the photons actually hits the plate serves as a starting point for an electron, the number of electrons that start from the position is simply adjusted by the calculated factor. As the enhancement factor is not an integer value the number of electrons is generated from the integer part first and the fraction that is left will be randomly determined, so that the electron will be produced with a certain probability. As an example, there will be two electrons and a third one with a probability of 60 % if the enhancement factor is 2.6. At this point it should be noted, that by this calculation, a photon to electron conversion under perpendicular penetration of 100 % is implied. This might be a realistic magnitude considering a caesium iodide coating, but the more practical advantage by this is the fact that at least one electron is produced per hit on the plate and by that a lot of calculation and thus computation time is saved. Approaching an angle of 0° the factor reaches infinity which would be a problem for the simulation. Due to the limited amount of energy the photon might transfer to the material and thereby to the electrons, the maximum number of "secondaries" can be calculated and used as a threshold. In section 3.2 the energy gap an electron must overcome to leave the material is defined by the bandgap or work function. In this case the value for caesium iodide was taken into the simulation, because the cathode plate for the experiment was later coated with a Caesium Iodide layer (compare 7.4). Thus, a value of 6.4 eV was taken into the calculation, leading to a maximum number of electrons of $N_{\max}(E_{\text{photon}}) = \frac{E_{\text{photon}}}{6.4}$ [27]. The energy of the photons $E_{\text{photon}}$ depends on the photon emission angle $\theta$ and can be calculated via equation 5.

After generating the start distribution for the electrons, the second simulation step could be developed. For the electrons that start their movement on the surface of the cathode plate, the start energy and the start angle are crucial input parameters. Beginning with the energy of the electrons the distribution discussed in section 3.2 has to be implemented. As one can see, the model derived by Henke *et al* [17] cannot describe the distribution in all detail and thus an experimentally measured distribution from a different work by Henke [16] was taken. Here distributions were available for different photon energies. The distribution for the lowest photon energy of 277 eV was taken since it came closest to the photon energy in the experiment at ESR of about 170 eV. The data was read from the

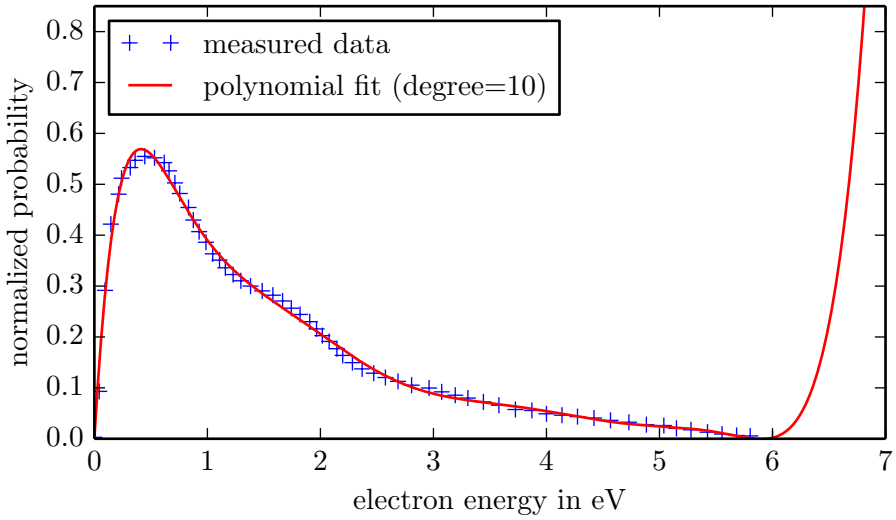


**Figure 22:** Measured secondary energy distribution by Henke *et al* [17] with a high order polynomial fit of degree 10. The fitted model was used up to an electron energy of 6 eV to randomly generate starting energies for the electron simulation.

| a | b | c | d | e | f | g | h | i | j |
|---|---|---|---|---|---|---|---|---|---|
| 3.7905 | -9.2171 | 10.6987 | -7.2470 | 3.0683 | -0.8341 | 0.1452 | -0.0156 | 0.0009 | -0.00002 |

**Table 1:** Parameter output from non-linear least squares fit of the experimental data by Henke *et al* [17].

picture, enabling an evaluation of the shape. Therefore, the data was fitted with a high order polynomial up to the tenth degree for a good approximation of the points. Figure 22 shows the experimental data by Henke and the polynomial fit which was used up to an energy of $E = 6\,\text{eV}$. The parameters from the non-linear least squares fit from the python package `scipy.optimize.curve_fit` are stated in table 1. The high energetic part of the spectrum, i.e, the primaries, was not implemented here, because it contains only about 1 % of the total number of electrons.

The fitted model was then embedded in the simulation such that electron energies according to the distribution are generated. The collected amount of 3000 photons from a total number of 60000 simulated photons result in an amount of approximately 7008 electrons due to the enhanced yield under flat angles (compare section 3.2). This is a factor of

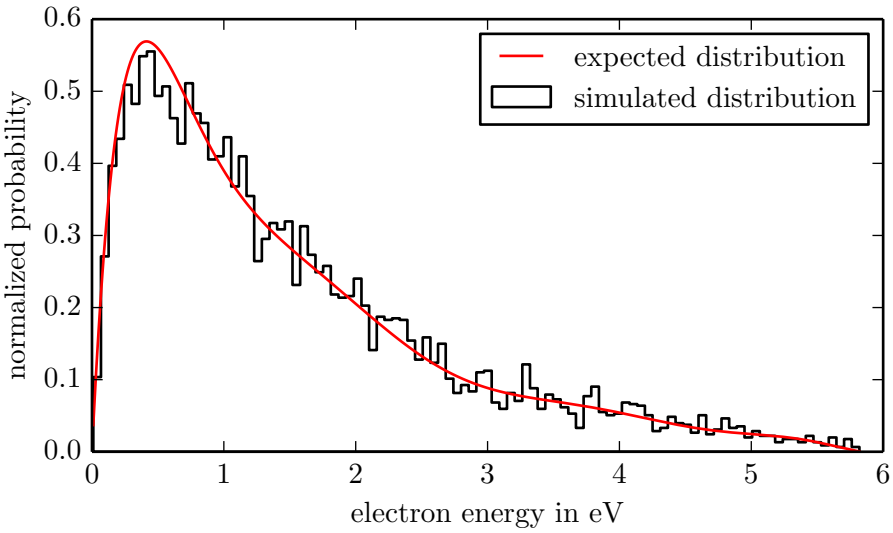


**Figure 23:** Graph of the fitted curve from figure 22 with data from the simulation of $\approx$ 7000 electrons. These electrons were created by an initial number of 60000 photons.

$$l = \frac{7008}{3000} = 2.34 \approx \frac{1}{\sin(25°)}. \tag{17}$$

This is in good agreement with the mounting angle of the cathode plate of 30°, because flatter angles stronger contribute to the overall yield that the steep angles due to the hyperbolic course of equation 16. So the average enhancement has to lie slightly above that for an angle of 30°. It has to be tested whether the amount of 60000 simulated photons is sufficient to generate enough electrons for a proper reproduction of the energy distribution. The histogram from the simulation is shown in figure 23 together with the expected distribution from the polynomial curve. The curve is not as well reproduced as it is for the photon angle distribution in figure 20 but the histogram clearly replicates the given distribution. This is due to the fact that the photon sample is significantly higher than the electron sample.

After implementing the presented procedures, it was investigated how big the overall error of the simulation is. The standard deviation gives a good approximation of the intrinsic error of the simulation. As in most cases, the standard deviation should decrease with the sample size $n$ following

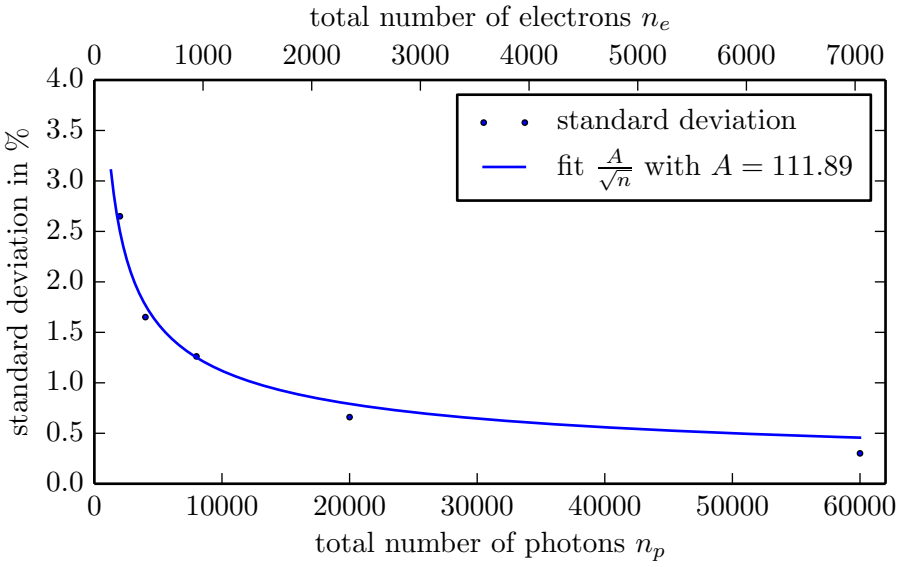


**Figure 24:** Investigation of the dependency of the standard deviation of the simulation results from the number of initially launched photons. The data points were fitted with the given formula in equation 18.

$$\sigma \approx \frac{1}{\sqrt{n}}. \tag{18}$$

To investigate this dependency the simulation was repeated 15 times for different numbers of photons and a fixed set of all other parameters. From the 15 outputs the standard deviation was taken and plotted against the initial number of photons and thereby produces electrons, respectively. Figure 24 shows the results for five different amounts of photons up to the previously used number of 60000. On the second $x$-axis the average number of simulated electrons by these photons is shown. One can see that the standard deviation of the simulation results decreases down to a value of $\sigma \approx 0.3\,\%$ which indicates that the error through the deviations in the electron energy spectrum should not be significant. The given points were fitted with the square-root criterion from equation 18 plus a constant scaling factor $A$.

This model cannot be used to make any predictions about the uncertainties compared to the real experimental setting. This point will again be discussed in the next chapter, when the experimental data is compared to the simulation output. At least it is proven here, that the simulation generates reproducible results already with a small amount of photons and therefore with manageable computation time.

# 6 Experiments

## 6.1 LED measurements

After the construction of the detector first measurements with a UV-LED were carried out by Jonas Vollbrecht [20] and Florian Trittmaack [28]. Similar measurements were performed in the new vacuum chamber in this work. The idea behind the measurements is to apply a certain and fixed set of voltages to the detector and vary one parameter during the measurement. The resulting curve gives a good impression of the influence of this parameter and can be well overlaid with similar curves obtained by the simulations. The most interesting parameters with the highest influence on the guiding properties of the detector are the magnetic field strength and the potential applied to the cathode plate.

To perform these measurements the UV-LED was placed in the vacuum chamber close to the MCP shielding (see figure 11 in [28]). It was connected to a function generator via a BNC feedthrough. The device drove the LED in a pulsed mode by applying a rectangular voltage function. The LED was mounted such that it is orientated towards the cathode plate. Since the MCP detector will also register scattered photons and electrons generated at the illuminated electrodes and walls, the voltage at the cathode plate was switched between negative and positive potential. By applying a positive potential all electrons that are produced on the cathode surface will be recollected and thus not detected. The measured count rate is treated as background and is subtracted from the measurement with negative potential.

The first measurement was carried out by setting all voltages to the parameters given by Florian Trittmaack and are presented in table 2. Then the coil current was tuned from 0 A to a maximum of 3.7 A resulting in the graph displayed in figure 25. It shows the count rate in arbitrary units subject to the applied current to the solenoid coils indicated by the continuous blue line. The red dashed line shows the according simulation result which is scaled to fit the experimental data. As the exact number of photons in the experiment is not known, both data sets were normalized to 1 at a coil current of 1.5 A. This is due to the fact that the values for the number of photons emitted by the LED and the conversion efficiency of the cathode plate are unknown. The simulation assumed a Gaussian photon distribution emitted by the LED according to the investigation of the emission characteristics by Jonas Vollbrecht [20]. Both results are in good agreement with each other describing the slowly decreasing rate at the high current part of the curve and the oscillation like shape in the low current scheme. This is due to the cyclotron motion of the electrons and the asymmetric illumination of the cathode plate by the LED which

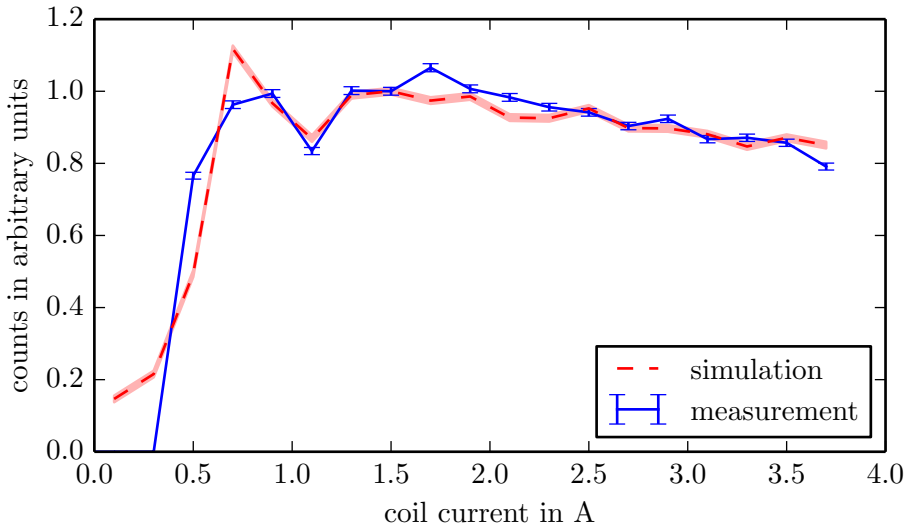


**Figure 25:** Measurement and simulation results with changing coil current for the measurements with the UV-LED. Simulated data is displayed with a $\pm\sigma$ band, where $\sigma$ was taken from figure 24 for an amount of 5500 electrons.

was already observed by Jonas Vollbrecht.

In a second measurements the coil current was set to a fixed value while the potential applied to the cathode plate was changed between values of $-100\,\mathrm{V}$ and $0\,\mathrm{V}$. The parameter set is shown in table 3 and the same measurement principle as before is used. The results of both the measurement and the simulation are presented in figure 26. The continuous line, again representing the measurement, shows a plateau until a voltage of $-40\,\mathrm{V}$ is reached, indicating the point where the electrons from the cathode plate do not gain enough energy through the accelerating potential at the cathode plate to overcome

**Table 2:** Parameter set for the measurements and the simulations as they were taken from Florian Trittmaack and used for the UV-LED experiments with different coil currents displayed in figure 25.

| Parameter | Value |
|---|---|
| Electrode 1 | $-25.1\,\mathrm{V}$ |
| Electrode 2 | $-22.4\,\mathrm{V}$ |
| Electrode 3 | $-101.4\,\mathrm{V}$ |
| Focus electrode | $0\,\mathrm{V}$ |
| Cathode | $-50\,\mathrm{V}$ |

| Parameter | Value |
|---|---|
| Coil current | 0 A - 3.7 A |
| MCP front | $300\,\mathrm{V}$ |
| MCP back | $2200\,\mathrm{V}$ |
| MCP anode | $2500\,\mathrm{V}$ |
| # electrons | 5500 |

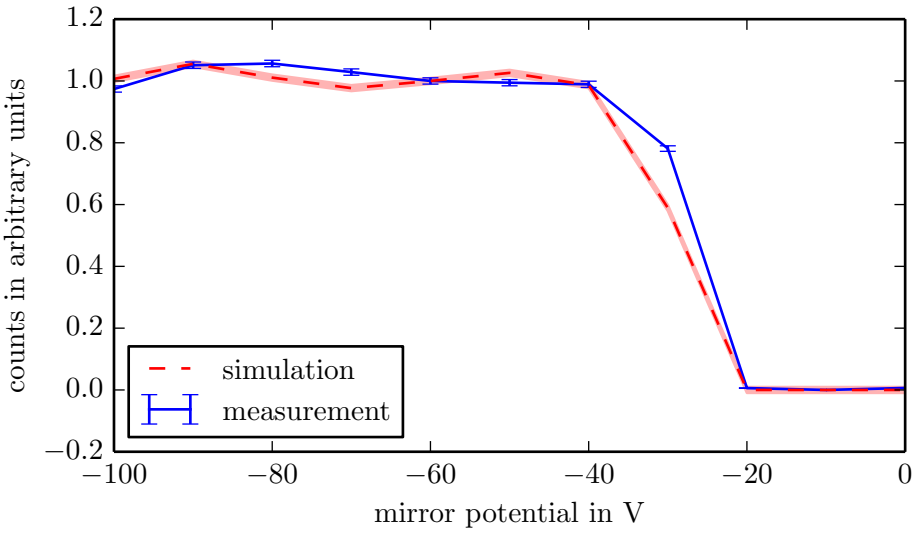


**Figure 26:** Measurement and simulation with changing mirror potential for the measurements with the UV-LED. Simulated data is displayed with a $\pm\sigma$ band, where $\sigma$ was taken from figure 24 for an amount of 5500 electrons.

the retarding potential of the ring electrodes or the focus electrode. The graph is in good agreement with the simulation indicated by the dashed line.

Both measurements are in good agreement with the previous ones performed by Jonas Vollbrecht and Florian Trittmaack. The good agreement with the simulations confirms that the implementation of the new model and also the further development of the program improved the simulation accuracy. It was mentioned that no absolute efficiency of the detector is known and thus the shape of the graph is a good validation for the simulations that were performed during the optimization processes described in section 7.1 and 7.2.

**Table 3:** Parameter set for the measurements and the simulations as they were taken for the UV-LED experiments with different mirror potentials displayed in figure 26.

| Parameter | Value |
|---|---|
| Electrode 1 | −50 V |
| Electrode 2 | −50 V |
| Electrode 3 | −50 V |
| Focus electrode | −90 V |
| Cathode | −100 V - 0 V |

| Parameter | Value |
|---|---|
| Coil current | 1.9 A |
| MCP front | 300 V |
| MCP back | 2200 V |
| MCP anode | 2500 V |
| # electrons | 5500 |

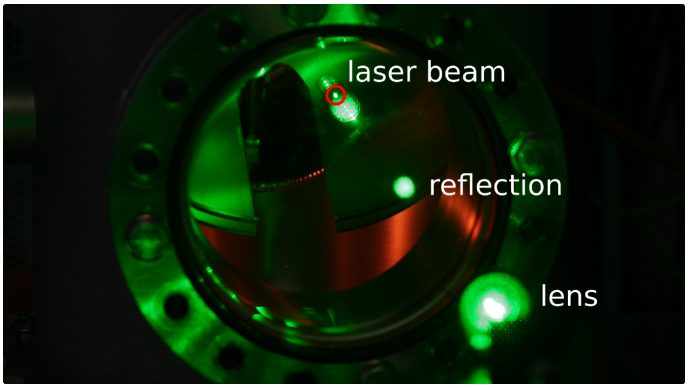


**Figure 27:** Picture of the adjustment of the laser setup with a green laser pointer. One can see the lens focusing the laser beam onto the cathode plate through the vacuum window.

## 6.2 Laser measurement

To improve the investigation of the photocathode, the UV-LED was replaced with a UV laser system. With the laser system it is possible to expand the measurements from a general understanding of the detector to a more detailed one by investigating different positions on the photocathode. The points on the cathode from which the magnetic field lines point onto the active area of the MCP can thus be precisely measured and compared to simulations. The laser has a wavelength of 266 nm which is obtained in a two stage frequency doubling process of a Nd:YVO4 laser. The beam is guided via an optical fiber to the setup and is then focused with an UV lens through the window at the side of the vacuum chamber (compare right flange in figure 15) onto the cathode plate. The holding to which the fiber and the lens is attached can be moved vertically and horizontally to scan a certain area on the cathode.

The laser spot could be moved a distance of 8 cm in the horizontal direction and 2.6 cm in the vertical direction. Due to the angle of the plate of 30°, this corresponds to an area of 8 cm × 5.2 cm on the surface of the cathode plate. Since the laser wavelength is in the ultra violet region, it cannot be seen on the cathode plate, thus the positional calibration was achieved with a green laserpointer which was radiated into the fiber. Figure 27 shows a picture of the cathode plate through the vacuum window. The green spot from the laser pointer can be seen on the cathode plate and was used to map the experimental position to the one of the model in the simulations.

The voltages and currents applied in the measurement are stated in table 4. As in the

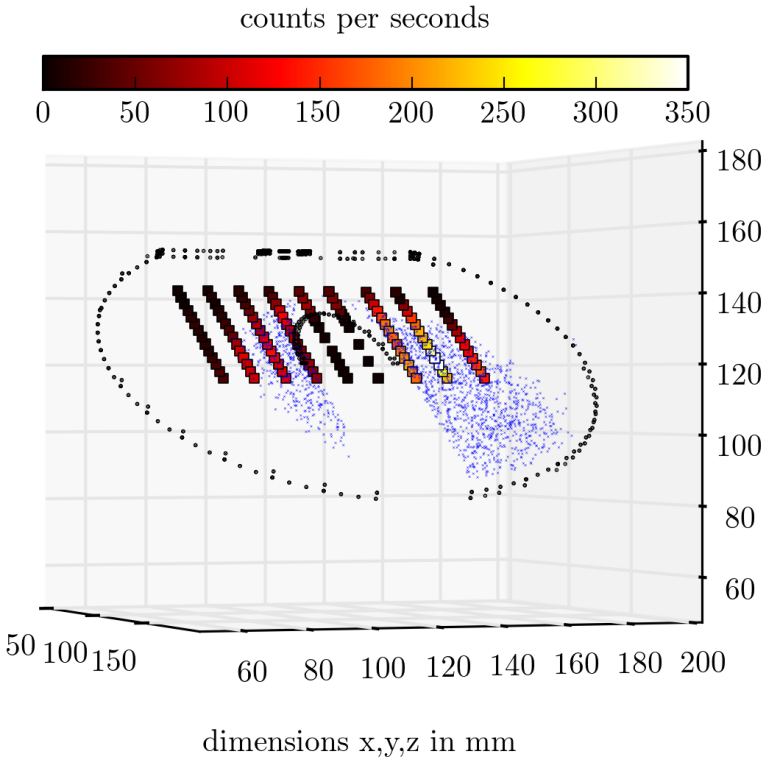


**Figure 28:** Laser measurements with the old cathode plate showing the count rate for different points together with the results from the simulation indicated by the dots showing the area that is imaged onto the MCP.

LED measurements, the voltage of the cathode plate was switched between positive and negative potential to distinguish background electrons and photons from electrons which originate from the cathode surface. The count rate for various positions was taken and displayed in figure 28. Parallel to the experiment, simulations were run in which electrons were launched all over the cathode surface under the same voltage and current settings of the experiment. All starting positions of detected electrons were taken and also plotted in figure 28 indicated by the green dots. Both the measured data points indicated by the quadratic boxes and the results from the simulations were mapped to the dimensions of the cathode plate of which the outline is displayed through the circular point structure. The measured data points are colored according to their count rate.

Figure 28 illustrates that the count rate in the measurement drops to zero when leaving the area indicated by the dots from the simulation. This shows that the simulated area

**Table 4:** Parameter set for the measurements and the simulations as they were used for the UV-Laser experiments.

| Parameter | Value |
|---|---|
| Electrode 1 | 0 V |
| Electrode 2 | −20 V |
| Electrode 3 | −100 V |
| Focus electrode | −50 V |
| Cathode | −50 V |

| Parameter | Value |
|---|---|
| Coil current | 1.9 A |
| MCP front | 300 V |
| MCP back | 2200 V |
| MCP anode | 2500 V |

from which electrons are guides to the MCP are in good agreement with the experimental results. With this result the problem of the old coil setup becomes clear. The size of the area that is imaged onto the MCP detector makes up only a small fraction of the whole cathode plate area. The overall shift of the area to the bottom right side is a result of the cyclotron motion of the electrons. As the magnetic field strength is very low in the area close to the cathode plate, the cyclotron radii of the electron trajectories are relatively high. When leaving the surface, the magnetic field forces the electrons into the same direction of rotation depending on the orientation of the magnetic field lines. The cyclotron radius $r$ can be calculated via

$$r = \frac{mv}{qB} \tag{19}$$

where $m$ denotes the particle mass, $v$ the particle velocity, $q$ the particle charge and $B$ the magnetic field strength. On their way up the field gets stronger, bounds the electrons tighter to the field lines and thus reduces the cyclotron radius. By this the electrons are overall shifted to one side and electrons that are not covered by the field lines pointing to the MCP will be detected while others covered by the field lines miss the detector. Additionally, the area of the slit that is indicated by the low rate in the middle, is in very good agreement with the real model of the slit showing that no electrons will be produced when missing the plate. This shows that the simulations cannot only explain a general behavior of the detector, but also very well reproduces the area that is covered by the magnetic field including the shift through the cyclotron motion.

Through the presented measurements with the LED and the laser, it could be proven that the experimental results are very well reproduced by the simulations. The previous chapter showed that the intrinsic error of the simulation is very low and thus results are replicable. Based on this it is possible to optimize the design based on the simulations, which will be the main goal of the investigation in the following chapter.

# 7 Optimization

This chapter will be about the optimization processes that were carried out in the course of this work. It will mainly follow the ideas, shortly introduced in section 4.4. The goal of this optimization process is to collect as many photons as possible on the cathode plate and also detect as many electrons as possible produced by these photons.

## 7.1 Improvement of the collection efficiency

The first thing that should be optimized is the design of the cathode plate. There are two open parameters that can changed, namely the size of the plate and the angle under which it is mounted to the carrier. The first is very intuitive as the plate should be made as big as possible to collect as much photons as possible. The constraining factor here is the size of the beam pipe at ESR since the plate must not hit the beam pipe when fully moved into the beam and also must fit into the connecting tube of the flange and the beam pipe when moved completely out of the beam. Before the dimensions of the plate can be set, the angle has to be chosen, because the maximal size also depends on the angle.

The angle of the plate has a huge impact on the guiding properties of the detector. The electrons are accelerated perpendicular to the cathode surface through the applied negative potential and thus a higher angle is directly connected to worse guiding properties. This becomes clear by regarding the direction of the acceleration. The MCP is placed perpendicular to the beam and thus a steeper angle results in a greater number of electrons that are accelerated further away from the detector. On the other hand significantly more photons will be collected at higher angles, because the effective area of the plate that is seen by the photons is greater. The trade-off between this two features and the and the enhancement factor $1/\sin(\varphi)$ are investigated in the following simulation process.

By increasing the angle of the plate one faces the problem that the setup gets more and more asymmetric. This can be attributed to the one-sided mounting at the carrier. To create a symmetric setup in the simulations, the cathode plate was moved to a centered position under the MCP. This is shown in figure 29, where three different plate configurations are shown. The first picture shows the given setup in which the plate is not placed in a central position under the MCP. This is changed in the second picture in which the plate is moved into the center of the setup. Keeping the plate in a central position but changing the angle results in the situation presented in the third picture. This approach was taken for the simulations to separate the effect of a changing angle from other effects such as the mentioned growing asymmetry. Furthermore, it is ensured that the slit is

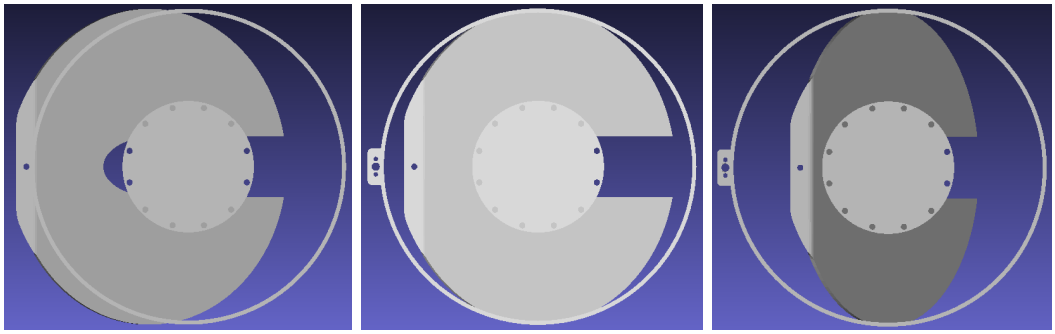

**Figure 29:** Different cathode plate configurations showing the asymmetric state of the cathode plate when mounted at the carrier in the left picture. The other two show states where the plate is moved in a central position under the MCP at different angles with respect to the beam line.

placed at the right position with respect to the beam line. By this setup it is achieved that the center point of the cathode plate is placed on the intersection point of the beam line and the MCP symmetry axis.

It is very important to note that the optimization process is highly dependent on the magnetic setup. Since the solenoid coil system should also be optimized, an intuitive setup was chosen as a first approach. The decision fell on a very simple design in which the old two coil system is replaced with only one coil which is shrunken to a minimum radius and is placed at the height of the MCP. This is reasonable, because the magnetic field lines can be tightened at the MCP and also cover a bigger area at the cathode as with the old coil system. The comparison between the magnetic field of the old coil setup and the one chosen for the angle optimization simulations is shown in figure 30. Only those field lines that point from the plate to the active area of the MCP are displayed.

The simulations for the final coil layout were performed after the angle and size of the cathode were fixed and will be presented in the subsequent section. With this interim solution for the coil setup, the simulations were carried out. Six models were created with cathode angles between 30° and 55°. All cathode plates had the same size and were moved to the center position under the MCP as shown in figure 29.

The simulations for the new angle were carried out when only some presented features from section 5.3 were implemented into the simulation program. Missing processes were the enhancement of the electron yield due to non-perpendicular impacting photons and the secondary electron energy distribution. The enhancing factor could be incorporated into

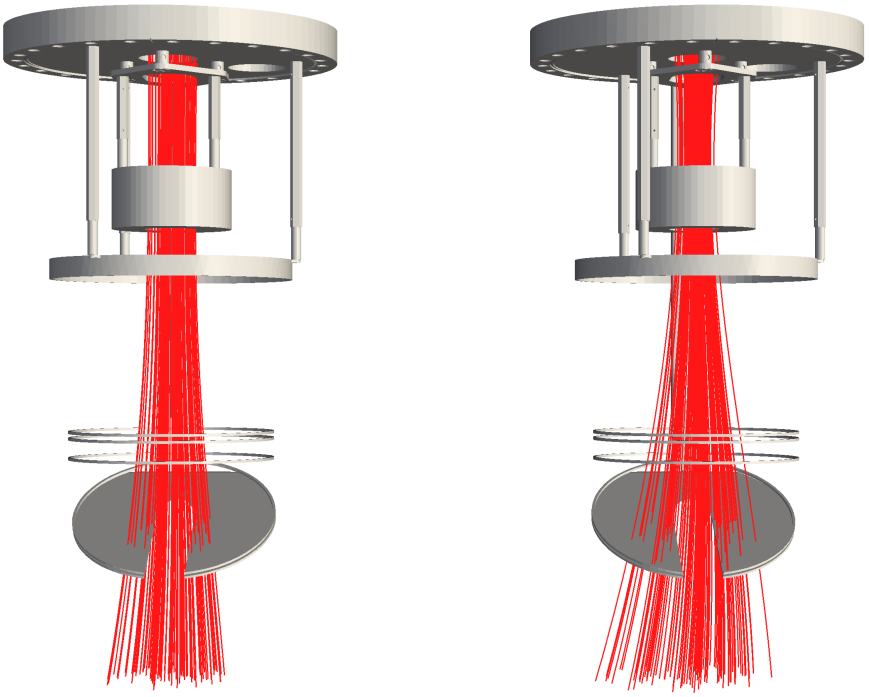

**Figure 30:** Comparison of the magnetic field created by two different coil geometries. Left: field lines created by the old two coil system; right: field lines created by one coil with a small radius at the height of the MCP.

the results afterwards by weighting every electron with the factor that can be calculated from the incident angle. The $N_{\max}$ was chosen to be $\frac{125\,\mathrm{eV}}{6.4\,\mathrm{eV}}$ from a medium value for the wavelength distribution of the photons of $\approx 10\,\mathrm{nm}$. This should not make a huge difference, because the effect would be nearly the same for all the different angles in the setup. The initial electron energy was set to 2 eV which is a good approximation for the electron distribution. Figure 31 shows the output for the different simulations. The simulations were carried out with the parameters given in table 5 measuring the collection efficiency in arbitrary units in dependence of the coil current which was altered between 2 A - 5 A. For comparison the same graphs are presented in figure 32 without the incorporation of the enhancement factor. The effect can clearly be seen as the whole graph is twisted.

As said, the angular enhancement factor is incorporated in the graphs in figure 31 compensating the smaller number of collected photons for flatter angles. From the results the 30° cathode plate still seems to be the optimal choice. Aside from the 35° plate all other angles seems to be significantly less optimal. The final decision fell on the 35° version of the plate, because it lies only slightly below the 30° version and additionally offers the

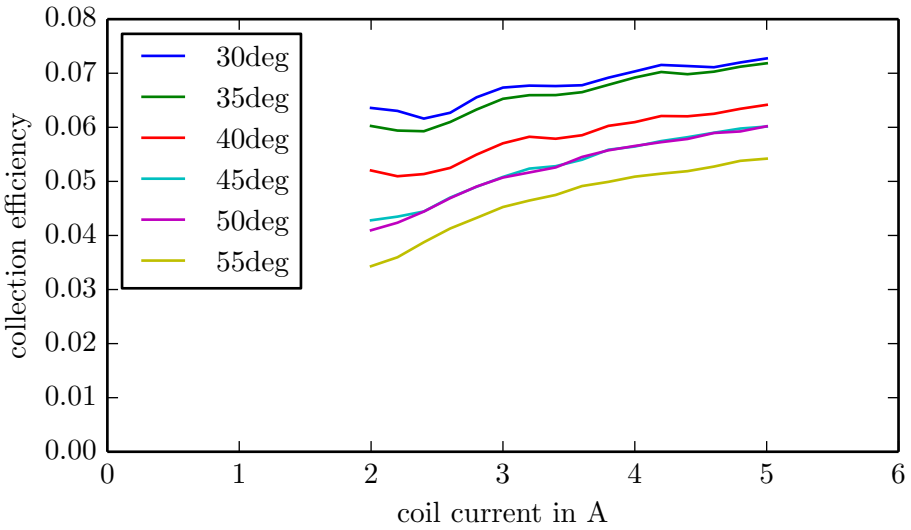


**Figure 31:** Simulation results for the angle optimization, showing six graphs, each representing a certain cathode angle. With the given parameter set in table 5 the current was altered producing the collection efficiency in arbitrary units depended of the coil current with the incorporated enhancement factor.

possibility to enlarge the plate. The second one is of major interest especially if the photon rate in the experiment is very low. Then it is advantageous to collect as many photons as possible to even generate a small signal which can be detected by the MCP as to miss the few emitted photons.

In the course of the optimization and the change of the angle, the ring electrode which was mounted directly above the cathode plate was removed, because it was fixed to the carrier and the angle or size could not be changed or adjusted to the new cathode plate. The new plate was developed by Hans-Werner Ortjohann, who also fitted the slit size to the

**Table 5:** Parameter set for the angle optimization simulations carried out for six different angles between 30° and 55°.

| Parameter | Value |
|---|---|
| Electrode 1 | 0 V |
| Electrode 2 | −20 V |
| Electrode 3 | −100 V |
| Focus electrode | −50 V |
| Cathode | −50 V |

| Parameter | Value |
|---|---|
| Coil current | 2 A - 5 A |
| MCP front | 300 V |
| MCP back | 2200 V |
| MCP anode | 2500 V |
| #photons; #electrons | 410000; 20000 − 28000 |

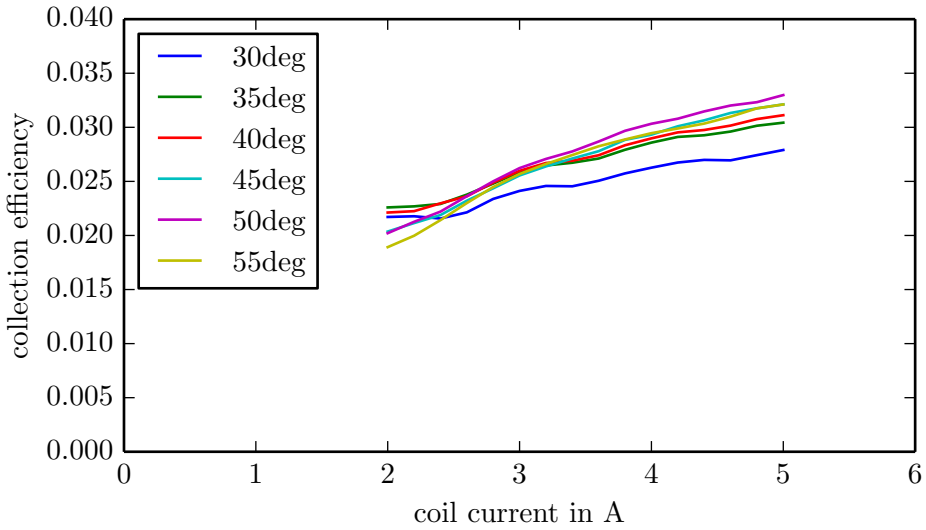


**Figure 32:** Graphs from the same data set as in figure 31 without the enhancement factor $1/\sin\varphi$.

new cathode position with respect to the ion beam. The constructed plate, corresponding to the new design is shown in figure 33. The thereby changed detector setup was implemented into the simulation to again compare some measurements that were carried out with the new layout (compare section 7.3 and section 7.4).

## 7.2 Optimization of the coil setup

As already mentioned before, the coil system, as it was used for measurements in the laboratory, was not matched to the detector. Hence, this section will deal with the adjustment of the coil system to achieve the best possible guiding of the electrons to the MCP. The development has to be carried out under some restrictions from the dimensions of the detector and the maximally allowed field strength in the beam pipe. The latter one is due to the fact that the magnetic field close to the ion beam must not exceed a value of 8 Gs to not disturb the ion beam in the ESR. The other one sets some minimal values for the size of the coils and accounts for the fact that the coils are mounted outside the vacuum and have to fit around the flange and the connection pipe at ESR. Through this the minimal inner diameter for the coils is 265 mm under the proposition of $\approx 6$ mm free space between flange and coils for the assembly. Through the surroundings at ESR it is only possible to mount the coil around the detector if the outer diameter of the coil does not exceed 325 mm. Also, the height of the coil is restricted to a maximum of 40 mm.

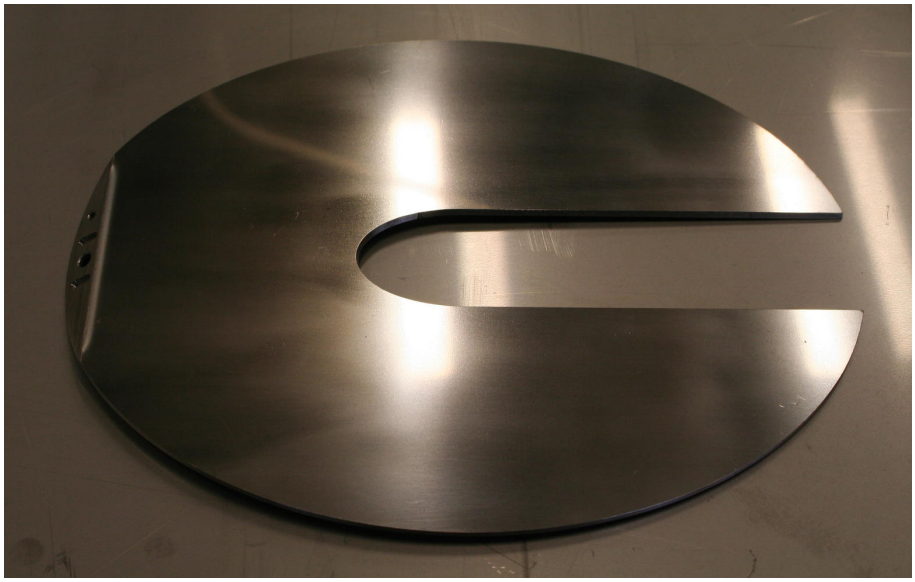

**Figure 33:** Picture of the manufactured photocathode with the newly developed design.

A scheme of the mounting flange and the important surroundings is presented in figure 35.

In the process of the angle optimization in section 7.1 the old coil system was replaced by one small coil mounted at the height of the MCP. This is quite intuitive since the magnetic field lines are tightest directly in the center of the coil, and the smaller the radius the wider the field lines at the cathode plate. The problem with this setup is that the field lines created by this coil still cover only a small part of the cathode plate (compare figure 30) and that this configuration is already the best possible solution with a single coil. The idea is to change again to a two coil system where the current in the bottom coil is applied counter-rotating to weaken the field and thus opening the field lines at the plate.

To get a impression of the course of the field lines when applying the counter field, figure 34 shows the field without the lower coil, with a small current through the second coil and finally with a high current through the second coil. The left two pictures show the field lines which hit the active area of the MCP, thus showing approximately the area on the cathode plate imaged onto the detector. When a small current is applied to the second coil, the field is damped and the field lines cover almost the complete cathode plate. Raising the current to a higher level, at some point the lower field becomes so strong that the upper field is completely compensated. At this point none of the electrons will reach the MCP. Between the state with the broad field at the plate and the state were the field is

**Figure 34:** The picture shows three different configurations for the coil system. In the left one the field is created by a single coil covering only a small area of the cathode plate. The middle picture indicates the field for a two coil system where a small counter-rotating current is applied to the lower coil thus the field lines cover most of the cathode plate. The right picture shows the total compensation of the field by the lower coil, guiding the electrons away from the MCP.

completely compensated, the optimal design has to be found under variation of four parameters, namely the current and the position of the upper and the lower coil. Since the solenoid coils in SIMION do not have radial dimensions, the diameter of both coils is set to 280 mm to approximate a real coil which turns will cover $\approx 30$ mm in the radial direction.

The top coil was placed at two different positions, one exactly at the height of the MCP and the other 50 mm above the MCP. The lower coil position was altered through many positions covering the whole possible range along the connection tube at ESR. Also, both coil currents were varied. In the course of the investigation it was observed that the best result can be achieved by turning off all electrode voltages except for a setting of $-5$ V at the cathode plate. A summary of the simulation parameters is given in table 6. For this scenario a uniform electron distribution on the cathode plate was chosen to get an impression of the collection efficiency from the whole surface free from different electron density effects.

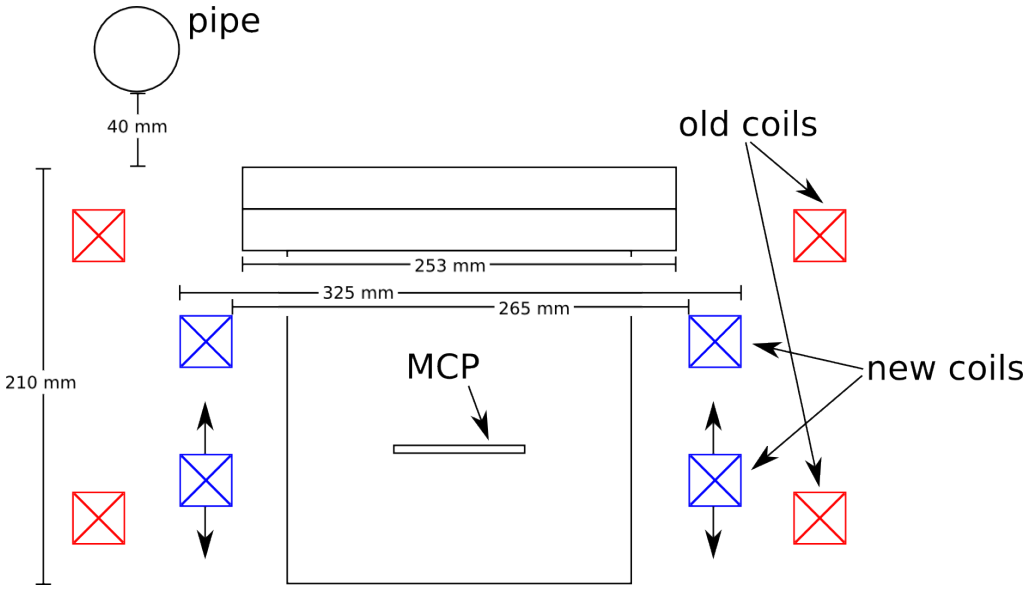


**Figure 35:** Schematic view of the ESR setup, which is important for the coil design. The old and new coil systems are displayed in the setup with their dimensions.

It also has to be noted that the simulation was changed significantly by implementing the experimental surrounding at ESR. This includes the connection tube, the beam pipe and also some other features at ESR around the detector. The close surroundings of the detector are of major importance, because these parts lay on grounded potential and alter the electric field lines significantly. The model that was implemented into the simulation is shown in figure 36. Apart from the mounting flange for the detector, it also includes other flanges around the detection region and especially a small part of the beam pipe. The complete model, which covers a big part of the beam pipe around the detector, was not implemented here since it would use too much memory to perform results in manageable computation time.

Figure 37 shows the results from the simulations with the top coil placed 50 mm above the MCP. Each of the plots corresponds to a certain current for the upper coil and shows the detection efficiency depending on the position and the current of the lower coil. A certain reappearing structure can be made out in all the pictures. With raising current of the upper coil it moves to the bottom left side of the plot. This can be understood since the higher the magnetic field created by the upper coil, the higher the lower field has to be to effectively open the field lines. Additionally, the maximally reached efficiency slightly rises with higher currents applied to the two coils. When the overall field gets stronger,

**Table 6:** Parameter set for the simulations concerning the new coil setup. Coil currents as well as coil positions were varied for both coils.

| Parameter | Value |
|---|---|
| Electrode 1 | 0 V |
| Electrode 2 | 0 V |
| Electrode 3 | 0 V |
| Focus electrode | 0 V |
| Cathode | −5 V |
| MCP front | 300 V |
| MCP back | 2200 V |
| MCP anode | 2500 V |

| Parameter | Value |
|---|---|
| Upper coil current | 4 A; 6 A; 8 A; 10 A |
| Lower coil current | −3 A to 0 A |
| Upper coil radius | 140 mm |
| Lower coil radius | 140 mm |
| Upper coil position | 0 mm; 50 mm above MCP |
| Lower coil position | −90 mm to 0 mm below MCP |
| # electrons | 5500 |

but the shape of the field lines stay the same, the electrons will be bound tighter to the field lines in their motion to the MCP. This will guide more electrons onto the active area of the MCP and thus explains the rising of the maximal achievable collection efficiency. Taking the highest value from the bottom right plot, the magnetic field strength reaches the limit of 8 Gs, hence no simulations with higher currents were conducted.

Since the detection efficiency with no current through the lower coil exactly represents the setup with no second coil at all, it can be noted that an enhancement from around 50 % to nearly 80 % can be achieved through the second coil. This shows that the field lines in this setup cover most of the cathode plate as already indicated in figure 34. The other two situations from figure 34 can also be found in the plots. The diagonal structure indicates the area where the influence of the lower coil is most effective, thus referring to the magnetic field lines in the second case. When the field is completely compensated (third picture in figure 34) the efficiency drops significantly since the field lines do not hit the MCP any more. This is the case for the bottom left area in all the four plots.

The preceding simulation was repeated with almost the same parameters, this time placing the upper coil at the same height as the MCP. Thereby the range for the second coil decreases which is indicated through the hatched space. All other parameters stayed the same, so table 6 provides all necessary information. Here it can be seen that the overall rate is lower compared to the previous simulation, but the structure is mostly the same. Additionally, the field strength at the plate succeeds the limit of 8 Gs in most cases. No further investigations were done here, because the previous setup was obviously better. Moving the top coil further above the MCP would create mechanical problems with the mounting of the coils due to the CF200 flange.

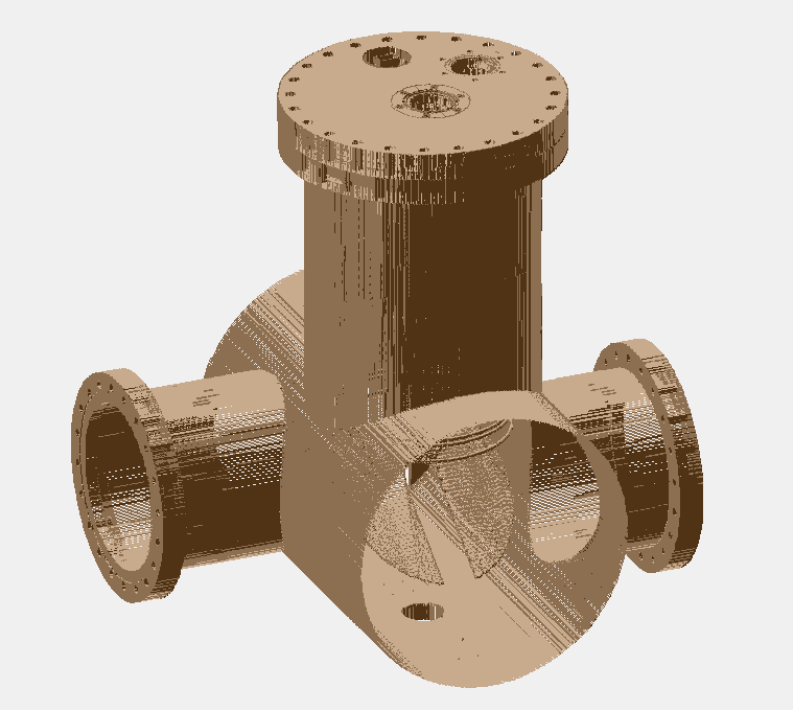

**Figure 36:** Detector model for the coil optimization simulations. The detector is placed inside the beam pipe from which the important features in the close surrounding of the detector are implemented.

In both measurements it becomes clear that the rate is the highest when both coils are close together. This is not easy to understand since different processes play a role here and their impact is not easy to estimate. The first one is the effect of magnetic reflection which takes place when the ratio of the field strengths at certain points is very high and the electron has a high angle between the field line and the direction of movement. When the coils are far away from each other, the second coil produces a significant kink in the field at which the electrons are reflected. Placing the coils close together will weaken the field under the lower coil but does not create such a significant kink. When the bottom coil is placed close to the MCP the acceleration of the electrons in the area of the field kink is high and thus magnetic reflection is suppressed. The phenomenon of magnetic reflection is based on the transfer of longitudinal momentum to the transversal component, eventually reflecting the electron. Accelerated electrons gain longitudinal momentum and are thus not reflected.

As the simulations clearly show a higher electron collection when the top coil is placed

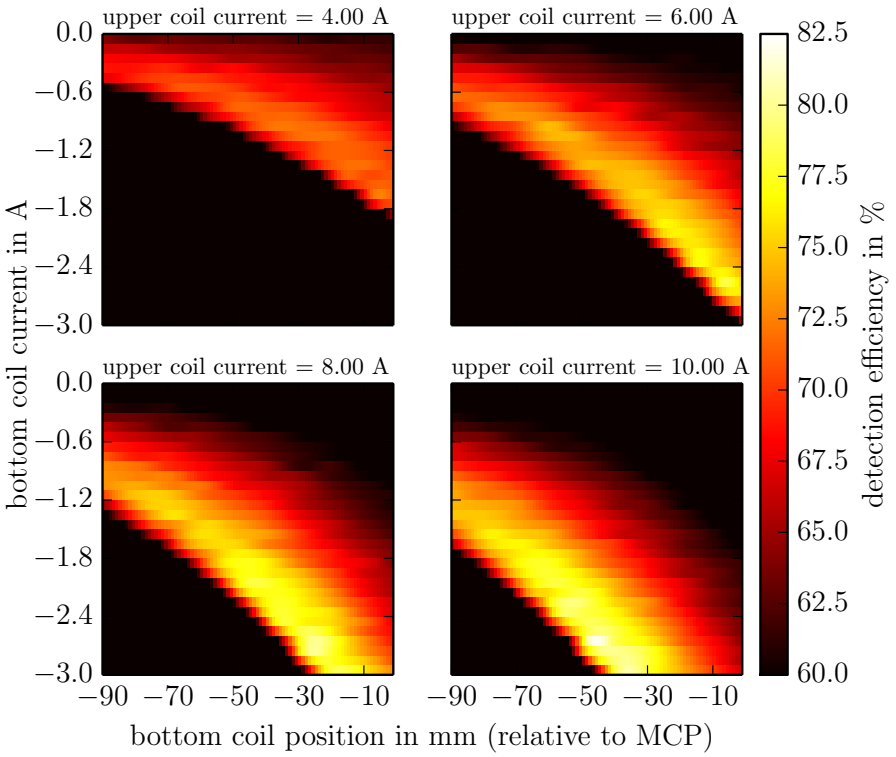


**Figure 37:** Results from the simulation with the top coil placed 50 mm above the MCP. Every plot represents the variation of the coil current and the coil position for the lower coil at a certain current of the upper coil. Simulation parameters can be taken from table 6.

above the MCP, this setup is the preferred one. For the final production of the coils it is crucial to investigate the temperature behavior, since the coils should be stable for long time measurements. This will be the crucial point for choosing the proper current for the upper coil. The simulation clearly indicates that a higher current leads to a higher electron collection efficiency. Thus, the limiting factor will be the temperature.

## 7.3 Laser measurement

This section will deal with a laser measurement which was already performed with the old detector setup from section 6.2. This time the measurement was carried out with the newly developed cathode plate. To ensure a good comparability between the two measure-

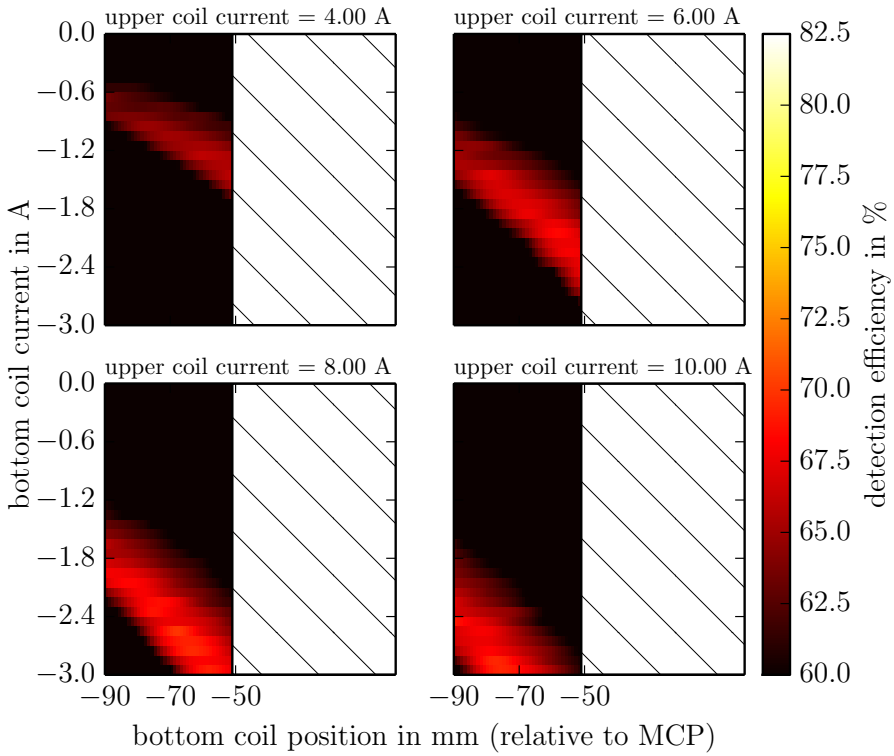


**Figure 38:** Results from the simulation with the top coil placed at the same height as the MCP. Every plot represents the variation of the coil current and the coil position for the lower coil at a certain current of the upper coil. Simulation parameters can be taken from table 6.

ments, the parameter set for the experiment was chosen to be the same as in the previous one including the old set of magnet coils. So all the relevant measurement settings can be seen in table 4. Since the angle of the new cathode plate is slightly steeper, the area that is covered with the laser on the plate now is 8 cm × 4.5 cm. Figure 39 shows the results from the measurement as well as the data from the simulation. The rectangular boxes indicate the measured data and are colored corresponding to the count rate. The results are mapped to the simulation data which again is indicated through the green dots.

Again the area that is covered by the magnetic field in the simulation is in very good accordance with the measured results. The most significant difference between both results is the higher count rate for the new cathode plate which is approximately 4 times higher. Additionally, the new plate shows a significantly smaller background count rate, which

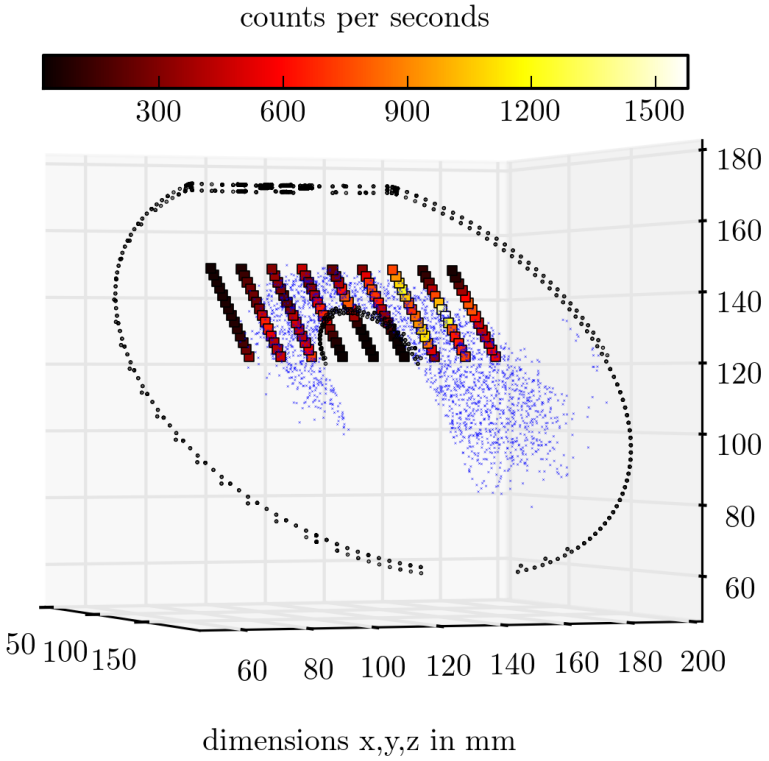


**Figure 39:** Laser measurements with the new cathode plate showing the count rate for different points together with the results from the simulation indicated by the dots showing the area that is imaged onto the MCP.

is in the order of 10 counts per second for each of the different points on the plate. In the measurements with the old plate the background rate was varying between 5 and 100 counts per second. Due to the smaller count rate, the fraction of scattered background photons or electrons is significantly higher in the old setup. This can be attributed to the surface roughness of the plate, since the new plate was surface polished whereas the old plate had a very rough surface. Whether the overall higher count rate of the polished plate can also be attributed to the surface roughness is unclear, but as nothing except the plate was changed in the setup, it is likely to be the reason for the enhanced electron yield.

In both measurements there is a specific place on the cathode where the rate is significantly higher compared to the other points. Here it cannot be distinguished whether there is a point on the MCP where especially many electrons will be detected or if there is a featured area on the vacuum window where fewer photons are reflected. In both measurements this

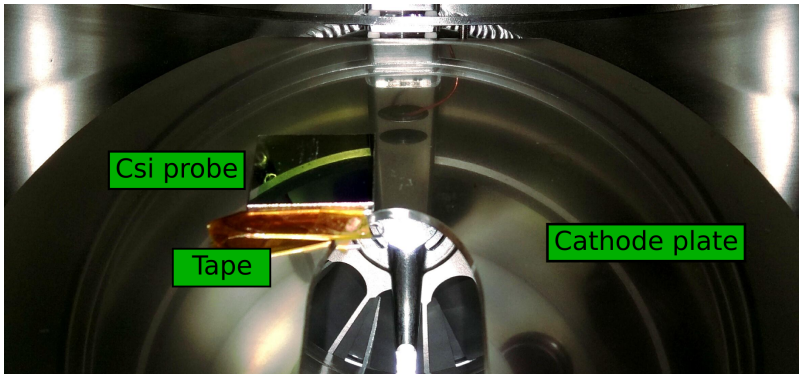


**Figure 40:** Photo of the coated steel probe attached to the cathode plate in the laboratory setup in Münster. The probe is fixed with a small piece of tape and electrically connected to the cathode plate.

area was measured twice to exclude fluctuations of the laser. Additional influences from the cathode plate can be excluded since the spot appears in the measurement with the old plate as well as with the new plate.

In comparison to the old plate, the area that is imaged onto the MCP is located at a different position with respect to the slit in the cathode. This is the case because the slit has a different length since the first ring electrode was removed from the setup and thus the plate is mounted higher at the carrier. The displayed volume is the same in both plots, so it becomes clear that the new plate is significantly larger than the old. The position of the plate as it is shown here is slightly shifted to the top of the plot. In the simulation the plate is placed correctly with respect to the beam line which is not the case in the laboratory setup in Münster. Here the cathode plate is a few millimeters to low. This will later be adjusted when the detector is mounted at the ESR with the small limitation screws restricting the movement of the pressured air motor. At this point it only has to be considered in the spatial evaluation of the data and will not alter the results.

## 7.4 Gamma source experiments

As indicated in section 3.2, the yield of photocathodes can be enhanced significantly by a caesium iodide coating. This was investigated in a lab experiment with a gamma source. Since caesium iodide has a cut off point for the production of electrons at a wavelength of $\approx 200\,\text{nm}$, the stated LED or laser from the previous measurements were not applicable. The value of 200 nm can be attributed to a secondary electron parameter of 6.4 eV in

**Table 7:** Results obtained by the gamma source measurements carried out by Daniel Winzen indicating an up to 7.7 times higher count rate for caesium iodide in comparison to stainless steel.

| Setup | Counts | Measurement time | Count rate |
|---|---|---|---|
| CsI probe | 60201 | 600 s | 100.3 Hz |
| no probe | 7784 | 600 s | 13 Hz |
| no probe | 14945 | 600 s | 24.9 Hz |

caesium iodide. This value is the sum of the bad gap $E_G$ and the electron affinity $E_A$ [27]. A possible alternative was a gamma source which emits photons with an energy of 8.04 keV. In the work of Samson [18] caesium iodide also shows a significantly higher electron yield as the metal gold for such high photon energies. So the source fits well to get a first impression of the electron yield from caesium iodide.

For this reason small steel probes with dimensions of 24 mm × 24 mm coated with a 300 nm thin layer of caesium iodide were produced. The caesium iodide was vacuum evaporated onto the steel plates in the target laboratory at GSI in Darmstadt [29]. Three probes were fabricated this way, where one steel plate had a rough surface whereas the two others were polished. One of the polished probes was implemented into the detector setup in the laboratory in Münster. Figure 40 shows the small probe in the vacuum chamber attached and electrically connected to the cathode plate. It is placed in a central position where it is covered by the magnetic field lines as this measurement was also carried out with the old coil system.

The mentioned gamma source produced an output of 2500 photons per second per steradian emitted into a cone of 0.5 sr. This data can be taken from the specification document [30] which also includes a drawing of the source. To produce an ever tighter output cone, the outlet nozzle was reduced with an aluminum plate from a diameter of 4 mm to 1 mm. This ensures that the photons mainly hit the small probe. From geometric considerations it is calculated that the fitted source emits 79 photons per second into a cone with a full opening angle of 11.5° which covers ≈ 200 mm$^2$ on the probe. The probe itself has the size of 576 mm$^2$. After adjusting the source in the vacuum chamber, the measurement was carried out with and without the probe. The measurement was performed by Daniel Winzen who obtained the results presented in table 7.

The measurement without the probe was carried out twice for two slightly different ori-

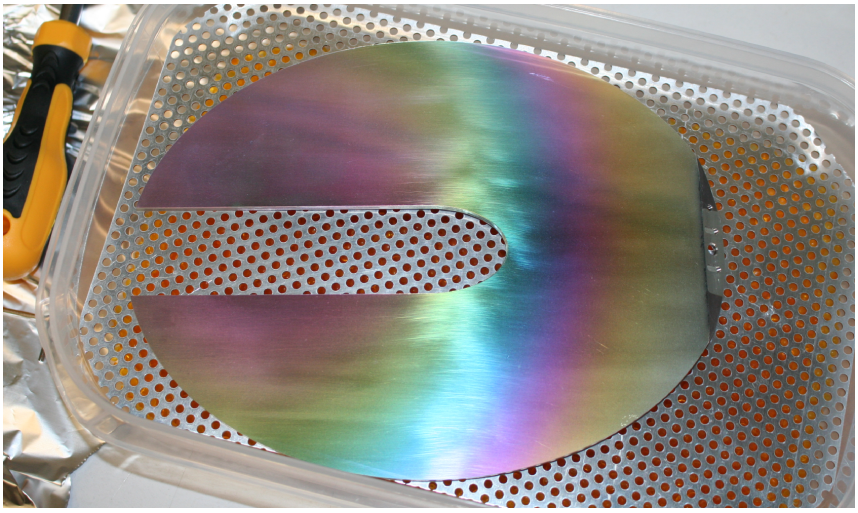

**Figure 41:** Cathode plate with a 300 nm thick vacuum evaporated caesium iodide layer creating a rainbow-like color structure at the surface.

entations of the gamma source. From the average of the two measurements, a 5.3 times higher count rate can be calculated when the coated probe is implemented into the detector. As the positioning of the source and also the estimation of the opening cone is quite uncertain, this data can be taken only as qualitative result and no analysis of the measurement error is performed. The count rate with the CsI probe (100.3 Hz) is higher than the expected photon rate (79 Hz) and thus the electron yield from the substrate is estimated to be higher than 1, which is in reasonable agreement with the result by Samson. As a rate as high as this is unlikely to be reached by stainless steel, it is highly probable that the probe has not been missed due to a false orientation of the gamma source.

Beside this investigation the other two probes were brought to the Institut für Optik und Quantenelektronik in Jena. Thy were investigated with a XUV laser source. First measurements also indicate a higher electron yield from caesium iodide in comparison to stainless steel. Nonetheless, no quantitative statements can be made at this point either.

The results of both measurements concerning the caesium iodide coating, together with the results from other authors introduced in section 3.2, indicate that the caesium iodide coating is superior to most other available coating for the XUV region. Based on these indications, the photocathode was coated with a $\approx 300$ nm thin layer of caesium iodide in the target laboratory at GSI just as the small probes before. The enhanced electron yield through the coating is not the only advantage of the coating. It might also reduce the background from optical photons due to the high secondary electron parameter of

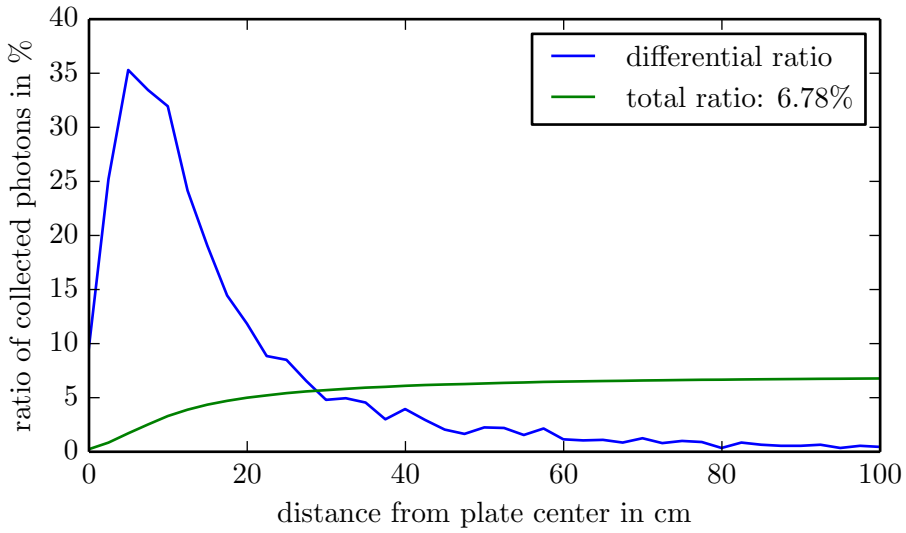


**Figure 42:** Ratio of collected photons for different distances from the cathode plate plus the integrated amount of totally collected photons showing an approximate total collection of 6.8 % of all the emitted photons within a distance of 1 m.

6.4 eV which corresponds to a cut off wavelength of 200 nm. Figure 41 shows a picture of the coated cathode plate. The thin layer generates a rainbow-like color structure on the surface of the plate.

## 7.5 Final detector parameters

This section will present some final parameters of the detector which will be important for the experiments at ESR. This will be the ratio of collected photons from the ions, the area that is covered on the cathode plate after the coil optimization and the time of flight distribution of the electrons.

The starting point will be the amount of collected photons. After the change in angle size of the cathode plate, the collection behavior along the beam line is investigated. From the graph in figure 42 it can be taken that approximately 6.8 % of the emitted photons over a distance of 1 m will be collected. Most of them from emitting points close to the cathode plate. With the old plate only 5 % of the photons were collected (compare section 5.3).

To get an impression of the covered area of the cathode plate, the start positions of all elec-

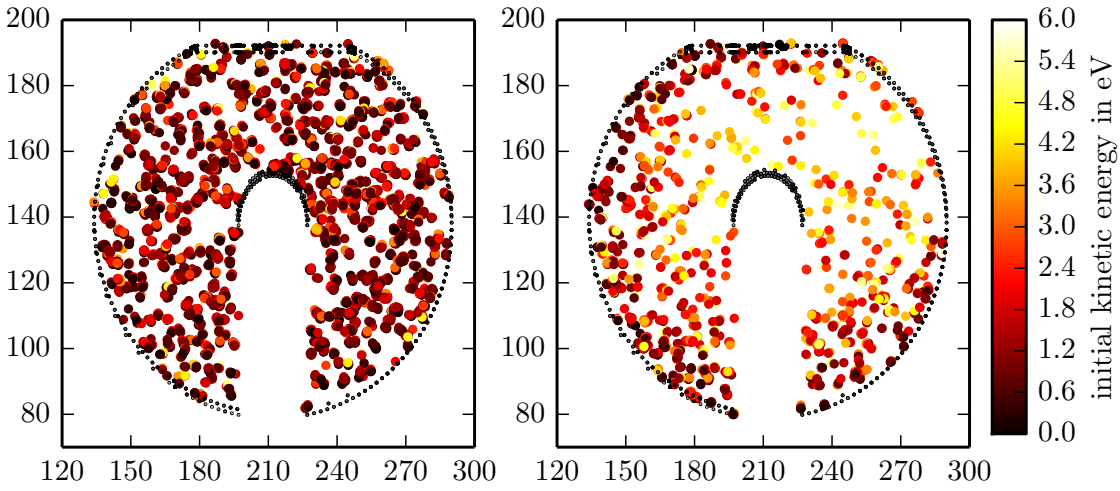


**Figure 43:** Covered area on the cathode plate. Left: start positions of all electrons that hit the detector; right: start positions of all electrons that do not reach the detector.

trons which are detected are displayed in the left picture of figure 43. On the other hand the positions of the electrons that do not reach the detector are shown in the right picture. The simulation parameters can be taken from table 8. It can be seen that electrons from all over the plate will be collected and guided to the MCP, which clearly indicated that the whole plate is covered by the magnetic field. This is a good result, considering the size restrictions of the coil system. Despite that, the electrons that do not reach the MCP are also distributed over the whole cathode but with a slight focus to the lower left part of the plate. Whether the outer parts of the plate are detected, is highly dependent on the initial start parameters and thus electrons with their kinetic energy vector pointing outwards will not be detected. The data points are colored according to their initial kinetic energy showing that most of the undetected electrons are from the high energy tail of the distribution from figure 22.

This can be explained with the effect of magnetic reflection which was shortly introduced in section 7.2. When an electron with a high angle to the field lines and a high kinetic energy starts on the plate, it has a higher probability to be reflected on its way to the MCP due to the momentum transfer. Nonetheless, close to 80 % of all the electrons will reach the detector.

Another very interesting property of the detector is the time of flight distribution of the

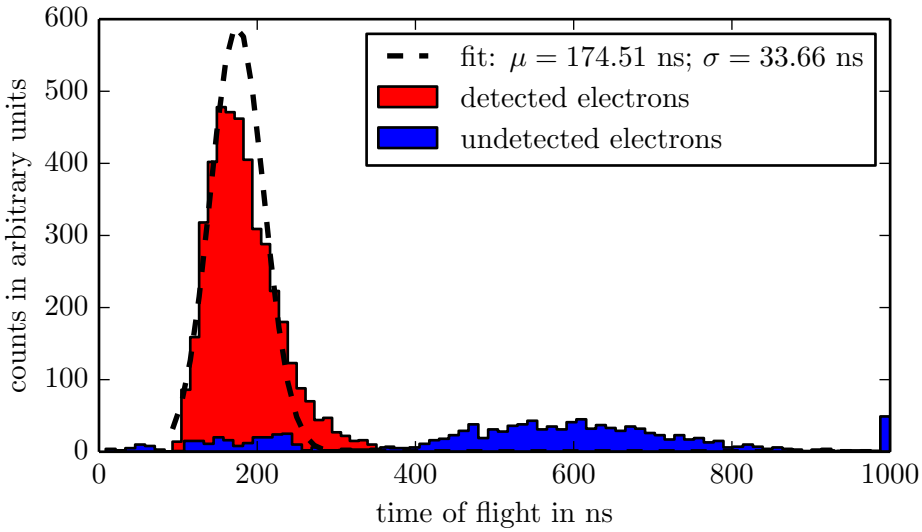


**Figure 44:** Time of flight distribution of the electrons showing the distribution for the detected and the non-detected electrons. A Gaussian function is fitted to the data for the detected electrons yielding a width of $\sigma = 33.66$ ns.

electrons. This is also a quite important value because the ion bunch in the experiment circles around the ESR with a frequency of $\approx 2$ MHz. Separated in two bunches with a measurement bunch and a reference bunch the frequency increases to $\approx 4$ MHz, which corresponds to a time of 250 ns between the bunches. Hence, the flight time distribution must be smaller to prevent overlaps between the bunches. Figure 44 shows the time of flight distribution for all the electrons, showing the detected ones in red and the undetected in blue. The simulation parameters were the same as for the investigation of the imaged cathode area presented in figure 43 and can be found in table 8.

Almost all the detected electrons have flight times between 100 ns and 300 ns depending on the start position on the plate. Electrons from the lower part of the plate, have a longer distance to the detector and thus a higher time of flight. A Gaussian distribution was fitted to the data resulting in a mean of 174.51 ns and a standard deviation of 33.66 ns. The width of the distribution is highly dependent on the electrode settings, in particular the voltage applied to the cathode plate. By changing the potential the electrons will be accelerated stronger and thus their time of flight reduces. This was also observed by Jonas Vollbrecht in his time of flight investigation with the old detector [20].

The undetected electrons mostly consist of the ones that hit the MCP shielding or are

**Table 8:** Parameter set for the simulations concerning the covered plate area and the time of flight distribution.

| Parameter | Value |
|---|---|
| Electrode 1 | 0 V |
| Electrode 2 | 0 V |
| Electrode 3 | 0 V |
| Focus electrode | 0 V |
| Cathode | −5 V |
| MCP front | 300 V |
| MCP back | 2200 V |
| MCP anode | 2500 V |

| Parameter | Value |
|---|---|
| Upper coil current | 8 A |
| Lower coil current | −2.4 A to 0 A |
| Upper coil radius | 140 mm |
| Lower coil radius | 140 mm |
| Upper coil position | 50 mm above MCP |
| Lower coil position | −30 mm below MCP |
| # electrons | 5500 |

magnetically reflected. They can be seen in the histogram as the accumulation around 200 ns and the one around 600 ns, respectively. The electrons that belong to the small peak at 1000 ns are those electrons that are excluded from the simulation after a flight time of 1000 ns. Most of them are circling electrons that are trapped in a periodic trajectory.

# 8 Summary and outlook

This work dealt with the final optimization of a given detector setup for spectroscopy measurements at the experimental storage ring at GSI. Several steps were performed to investigate the current behavior and influence of certain detector parts, especially the cathode plate, to finally create a reliable simulation program. Therefore, some physical properties such as the electron energy distribution, the photon angular distribution and also the emission characteristics of the ion bunch were implemented. This lead to simulations which were able to describe the experimental data quite well. These simulations were used to carry out simulations improving on the one hand the collection efficiency and on the other hand the magnetic guiding properties of the detector. Additionally, the effect of a caesium iodide coating was investigated in lab measurements. Through the simulations the angle of the cathode plate was changed from 30° to 35° to enhance the effective target size of the plate without compromising the guiding properties significantly. Furthermore, the size was maximized to achieve an even higher photon collection efficiency. The guiding of the electrons from the plate to the MCP could be improved by finding an optimized coil setup which is fitted to the detector. By a two coil system with counter rotating currents a configuration was developed which mostly guides all the electron created on the cathode plate to the detector leading to an electron collection efficiency of about 80 %. Finally, the measurements concerning the caesium iodide coating indicated a significantly higher electron yield as with plain steel.

As most of the optimizations were based on simulations and could not be tested experimentally up to this point, there is room for measurements to examine the behavior of the detector after the performed changes. Especially measurements concerning the electromagnetic setup are interesting, since the influence of the ring electrodes in the new setup is uncertain. The optimal currents for the solenoid coils, found through the simulations, have to be proven too. The detector is currently mounted at the ESR for a beamtime to test it in a laser spectroscopy measurement. A short introduction to this measurement is presented in the subsequent section.

## 8.1 Current state at GSI

After the stated optimization process, the detector was finally delivered to GSI. It was leakage tested in their vacuum laboratory and afterwards mounted to the ESR. Figure 45 shows a picture of the detector where it is mounted to the ESR. After the vacuum bake out, the MCP was put into operation and its functionality was successfully tested. A crucial point for the commissioning of the detector is the correct adjustment of the cathode plate

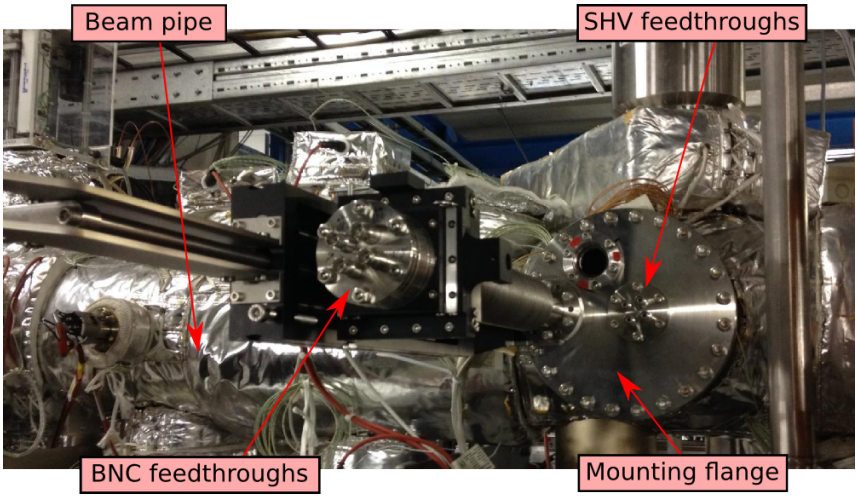


**Figure 45:** Picture of the detector mounted to the CF200 flange in the optical detection region at the ESR.

with respect to the beam line. The pressured air motor drives the detector into the beam and has to stop at the exact position, such that the slit is placed symmetrically around the beam. This was achieved by adjusting the micrometer screw at the axes table for the vertical position and the limitation screw for the pressured air motor for the horizontal orientation.

To indicate the position of the beam a telescope with a cross-hair pointer had been used to look through the beam pipe. With scrapers that were driven into the beam pipe, the position of the ion beam was indicated and the cross-hair properly adjusted. Then the detector was driven into the beam line and aligned according to the cross-hair. Figure 46 shows a schematic picture from the point of view of the telescope with indications for the scrapers and the detector with a shot through the telescope showing the illuminated cathode plate and the cross-hair. A picture of the telescope is also shown in figure 46.

The plate is placed such that the distance from the left edge of the slit to the ion beam is 15 mm and the distance from the horizontal edges of the slit to the beam is also 15 mm. This alignment places the cathode symmetrically around the beam line since the width of the slit is 30 mm. Therefore, the vertical micrometer screw is set to a position of 10 mm. From this point on the coil system has to be manufactured and mounted around the detector to run tests with the detector under controllable and realistic circumstances. For that the readout electronics have to be set up and configured. For this, the old readout system from the LIBELLE experiment will be used.

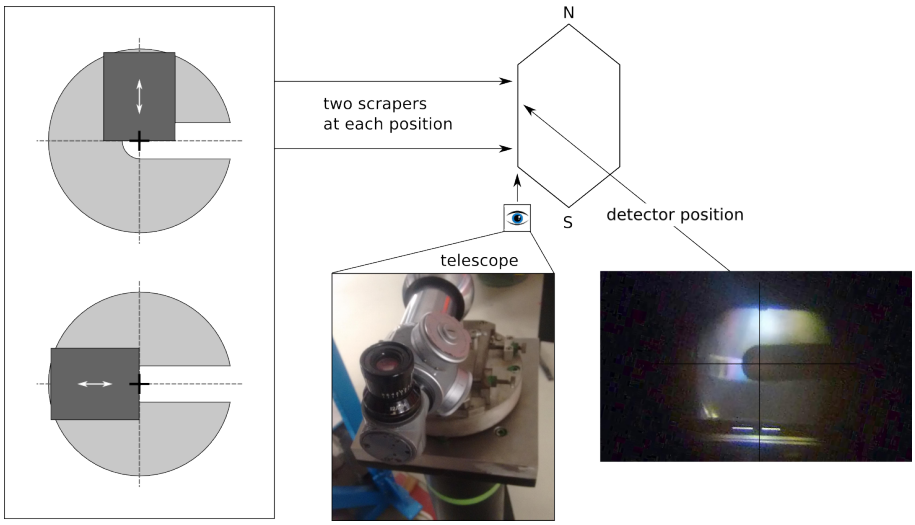


**Figure 46:** Scheme of the scrapers which are used to point the position of the ion beam in vertical and horizontal direction. They can be driven to certain positions and the cross-hair of the telescope can be adjusted to the exact position. The detector will then be orientated according to the cross-hair.

**Table 9:** Possible transitions of the lithium-like carbon ions for the test measurement. Data according to [31] and [32].

| transition | energy | wavelength |
|---|---|---|
| $^2p_{3/2} \rightarrow {}^2s_{1/2}$ | 7.994 86 eV | 155.0798 nm |
| $^2p_{1/2} \rightarrow {}^2s_{1/2}$ | 8.008 20 eV | 154.8216 nm |

In summer 2016 there will be a test beamtime at ESR in which the functionality of the XUV detector will be tested. The therefore used ions are lithium-like carbon ions ($^{12}C^{3+}$) moving around the ESR with a velocity of 0.47 c corresponding to an energy of 122 MeV u$^{-1}$. The ions will be excited with a wavelength of 257 nm by a pulsed laser source. The emitted photons have a wavelength of $\approx$ 155 nm in the co-moving system which is boosted to a wavelength of $\approx$ 93 nm in forward direction. Table 9 shows the two possible transitions of the carbon ions where the $^2p_{1/2} \rightarrow {}^2s_{1/2}$ transition will most probably be utilized. The detector is not optimized to a wavelength of 93 nm especially through the caesium iodide coating, but nonetheless the electron yield should still be significantly higher compared to stainless steel. It is in the order of 50 % (compare figure 9) thus the transition should be measurable by the detector. The final experiment E104 utilizing the beryllium-like krypton transition is planned to take place in 2018.

# 9 Literature


[1] R.K. Janev, L.P. Presnyakov, and V.P. Shevelko. Physics of Highly Charged Ions. *Springer Series in Electrophysics*, 13, 2012.

[2] E. Charro, I. Martín, and C. Lavín. MULTI-CONFIGURATION DIRAC-FOCK AND RELATIVISTIC QUANTUM DEFECT ORBITAL STUDY OF TRIPLET-TRIPLET TRANSITIONS IN BERYLLIUM-LIKE IONS. *Journal of Quantitative Spectroscopy and Radiative Transfer*, 56, 1995.

[3] Jörg Krämer. Aufbau und Test einer Ionenfalle für die Laserspektroskopie an hochgeladenen Ionen. *Institut für Kernchemie, Mainz*, 2007.

[4] Daniel D. Dietrich, John A. Leavitt, Harvey Gould, and Richard Marrus. Radiative decay of the $2p\ ^2\mathrm{P}_{3/2,1/2}$ states of lithiumlike krypton (Z=36) and the $2s2p\ ^3\mathrm{P}_1$ state of berylliumlike krypton. *Physical Review A*, 22, 1980.

[5] J.D. Gillaspy. Highly charged ions. *JOURNAL OF PHYSICS B: ATOMIC, MOLECULAR AND OPTICAL PHYSICS*, 34, 2001.

[6] R. Hutton, I. Martinson, B. Nystrom, K. Ando, Y. Awaya, P. Bengtsson, T. Kambara, Y. Kanai, T. M. Kojima, Y. Nakai, K. Ishii, and M. Jäger. Intercombination Transition in Beryllium-like and Boron-like Iron. *Physica Scripta*, 55, 1996.

[7] J. P. Marques, F. Parente, and P. Indelicato. Hyperfine quenching of the $1s^22s2p\ ^3\mathrm{P}_0$ level in berylliumlike ions. *Phys. Rev. A*, 47:929–935, Feb 1993.

[8] W. Demtröder. Laser Spectroscopy. *Springer-Verlag*, 2003.

[9] Vladilen Letokhov. Atomic Physics at Accelerators: Laser Spectroscopy and Applications. *Physica Scripta*, 68, 2003.

[10] K. T. Cheng, M. H. Chen, and W. R. Johnson. Hyperfine quenching of the $2s2p\ ^3\mathrm{P}_0$ state of berylliumlike ions. *Phys. Rev. A*, 77:052504, May 2008.

[11] D F A Winters. Laser spectroscopy of the $(1s^22s2p)\ ^3\mathrm{P}_0 - ^3\mathrm{P}_1$ level splitting in Be-like krypton. *Physica Scripta*, 2011(T144), 2011.

[12] V. Hannen et al. Detection system for forward emitted photons at the Experimental Storage Ring at GSI. *Journal of Instrumentation*, 2013.

[13] `https://www.gsi.de/work/beschleuniger/esr.htm`. [Online; accessed 29-03-2016].

[14] `http://web-docs.gsi.de/~stoe_exp/laboratory/environment/esr/esr.php`. [Online; accessed 28-06-2016].

[15] Burton L. Henke, Jerel A. Smith, and David T. Attwood. 0.1-10-keV x-ray-induced electron emission from solids - Models and secondary electron measurements. *Journal of Applied Physics*, 48, 1977.

[16] B. L. Henke, J. P. Knauer, and K. Premaratne. The characterization of x-ray photocathodes in the 0.1-10-keV photon energy region. *Journal of Applied Physics*, 52, 1981.

[17] Burton L. Henke, John Liesegang, and Steven D. Smith. Soft-x-ray-induced secondary-electron emission from semiconductors and insulators: Models and measurements. *Physical Review B*, 19(6), 1979.

[18] James A.R. Samson. PHOTOCATHODES: THEIR EFFICIENCY AND STABILITY. *Nuclear Instruments and Methods in Physics Research*, 222:215–220, 1984.

[19] A. Breskin. CsI UV photocathodes: history and mystery. *Nuclear Instruments and Methods in Physics Reserach*, 371, 1996.

[20] Jonas Vollbrecht. Lifetime analysis of the HFS states in hydrogen-and lithium-like bismuth and development of an in-beam detection system for extreme UV photons. *Institut für Kernphysik, Münster*, 2016.

[21] Denis Anielski. Entwicklung eines Detektoraufbaus zur Bestimmung der 2s-Hyperfeinstrukturaufspaltung von $^{209}Bi^{80+}$ am Experimentierspeicherring an der GSI. *Institut für Kernphysik, Münster*, 2010.

[22] Roentdek Handels GmbH. MCP detector with timing anode - Manual for MCP ToF detector DET40/75. Version 11.0.1601.2.

[23] `https://commons.wikimedia.org/wiki/File:Mcp-de.svg`. [Online; accessed 29-03-2016].

[24] Inc. Scientific Instrument Services. Simion package. `http://simion.com`.

[25] `https://www.winehq.org/`.

[26] `http://www.seos-project.eu/modules/laser-rs/laser-rs-c03-s02-p02.html`. [Online; accessed 17-02-2016].

[27] G. W. Fraser. THE CHARACTERISATION OF SOFT X-RAY PHOTOCATHODES IN THE WAVELENGTH BAND 1-300Å - II. Caesium iodide and other insulators of high photoelectric yield. *Nuclear Instruments and Methods*, 206:265–279, 1983.

[28] Florian Trittmaack. Optimierung eines XUV-Detektors, für den einsatz am experimentellen Speicherring, an der GSI. *Institut für Kernphysik, Münster*, 2015.

[29] GSI Helmholtzzentrum fr Schwerionenforschung GmbH. Target laboratory. `https://www.gsi.de/work/fairgsi/rare_isotope_beams/target_laboratory.htm`.

[30] Amersham Buchler. Variable Röntgenstrahl-Quelle.

[31] W.R. Johnson, Z.W. Liu, and J. Sapirstein. TRANSITION RATES FOR LITHIUM-LIKE IONS, SODIUM-LIKE IONS, AND NEUTRAL ALKALI-METAL ATOMS. *Atomic Data and Nuclear Data Tables*, 64(2):279 – 300, 1996.

[32] Charlotte E. Moore and Paul W. Merrill. Partial Grotrian Diagrams of Astrophysical Interest. *National Bureau of Standards*, 23, 1968.

## Danksagung

Mein erster Dank geht an Prof. Christian Weinheimer und Dr. Volker Hannen für das entgegen gebrachte Vertrauen zur Teilnahme an diesem Projekt und der damit verbundenen Masterarbeit. Darüber hinaus gilt der Dank auch für die Hilfe bei fachlichen, technischen aber auch organisatorischen Problemen, der sich auf die ganze Arbeitsgruppe erstreckt. Hier möchte ich Daniel besonders hervorheben, der mir in teilweise langen, bis spät in den Abend andauernden fachlichen Diskussionen und den damit verbundenen Denkanstößen sehr weiter geholfen hat.

Um namentlich niemanden zu vergessen, geht der Dank zusätzlich in gesammelter Form an die feinmechanische Werkstatt, die E-Werkstatt und an die Kollegen aus Jena und Darmstadt, die alle ihren Teil zu dieser Arbeit beigetragen haben.

Das vielleicht wichtigste für den Abschluss dieser Arbeit war die lustige und entspannte Atmosphäre auf dem Flur und in den Büros. Nicht nur beim Kaffee, sondern auch bei Filmabenden, Kinobesuchen, Grilltreffen am Aasee und vielen Anlässen mehr, habe ich nicht nur tolle Leute kennen gelernt sondern auch neue Freunde gewonnen.

Zu guter Letzt möchte ich mich bei meiner Familie und meinen Freunden bedanken, die in schwierigen Zeiten an meiner Seite gestanden haben und mir die Kraft gegeben haben jeden Stolperstein auf diesem Weg zu überwinden.

Auf die ewig gestellte Frage von Alex kann ich nun endlich wahrheitsgemäß antworten:

"Ja, ich bin fertig."